

Contents lists available at ScienceDirect

Energy

journal homepage: www.elsevier.com/locate/energy





Dynamic modeling and control strategy of an organic Rankine cycle with concentration regulation of the zeotropic mixture working fluid

Zheng Miao a,b,* , Yuchen Zhang , Peiwei Yan , Jinliang Xu a,b ,

- ^a The Beijing Key Laboratory of Multiphase Flow and Heat Transfer, North China Electric Power University, 102206, Beijing, China
- b Key Laboratory of Power Station Energy Transfer Conversion and System (North China Electric Power University), Ministry of Education, 102206, Beijing, China

ARTICLE INFO

Keywords: Organic Rankine cycle Dynamic modeling Concentration regulation Mixture working fluid Control strategy

ABSTRACT

Fluctuations in heat source/sink conditions degrade the performance of the organic Rankine cycle system and hinder its widespread application. The concentration regulation of the mixture working fluid is proposed in this work as a control approach to enhance the adaptability of the system to heat source/sink fluctuation. Two control strategies, constant-evaporation-pressure operation and constant-output-power operation, are investigated through the developed dynamic model of a 4-kW organic Rankine cycle prototype. The results indicate that, compared to the temperature glide of the mixture during phase change, a more significant mechanism of concentration regulation is the variation of the average evaporation and condensation temperatures. The trade-off between the exergy destructions of the evaporator and condenser results in the optimal system performance at a specific mixture concentration. The mixture concentration alongside the mixture mass flow rate enables dual-objective control of the system. The concentration-adjustable organic Rankine cycle exhibits superior performance in both constant-evaporation-pressure and constant-output-power operations compared to the fixed-concentration organic Rankine cycle and the basic organic Rankine cycle with pure working fluid in two aspects: the enlargement of the effective control range and the improvement of system performance. Under the fluctuation of heat source/sink conditions, the control range of the concentration-adjustable system is about 3-3.3 times wider than the fixed-concentration system, while the performance of the concentration-adjustable system is about 9.01 %-14.81 % higher in terms of the thermal efficiency and about 9.72 %-13.64 % higher in terms of the exergy efficiency than the basic organic Rankine cycle.

Nomenclature

Symbols		Greek	Greek symbols	
\boldsymbol{A}	area, m ²	η	efficiency	
а	chevron angle, rad	ρ	density, kg/m ³	
Bo	boiling number	λ	thermal conductivity, W/	
			(m·K)	
b	corrugation pitch, m	Subscr	ipts -	
c	specific heat capacity, J/(kg·K)	c	end-of-expansion state	
de	hydraulic diameter, m	cool	cooling water	
$M_{ m wf}$	mass flow rate of the working fluid,	e	evaporation	
	kg/h			
$N_{\rm exp}$	expander rotating speed, RPM	ex	exhaust, exergy	
Nu	Nusselt number	exp	expander	
P	pressure, kPa	f	fluid	
Pr	Prandtl number	g	gas	
Pd	back pressure, kPa	hf	heat source fluid	
Q	heat power, kW	i	inside	
			(continued on next column)	

(continued)

Re	Reynolds number	in	inlet
RPM	Units of rotational speed	1	liquid phase
s	specific entropy, J/kg·K	O	outside
T	temperature, °C	p	pump
t	time, s	tp	two-phase
U	Wetted perimeter, m	S	isentropic process
ν	specific volume, m ³ /kg	w	wall
w	specific power, kJ/kg		

1. Introduction

The increasing global energy demand leads to serious energy and environmental issues. Developing clean energy sources and improving energy efficiency have become urgent priorities [1,2]. Owing to its

^{*} Corresponding author. The Beijing Key Laboratory of Multiphase Flow and Heat Transfer, North China Electric Power University, 102206, Beijing, China. E-mail address: miaozheng@ncepu.edu.cn (Z. Miao).

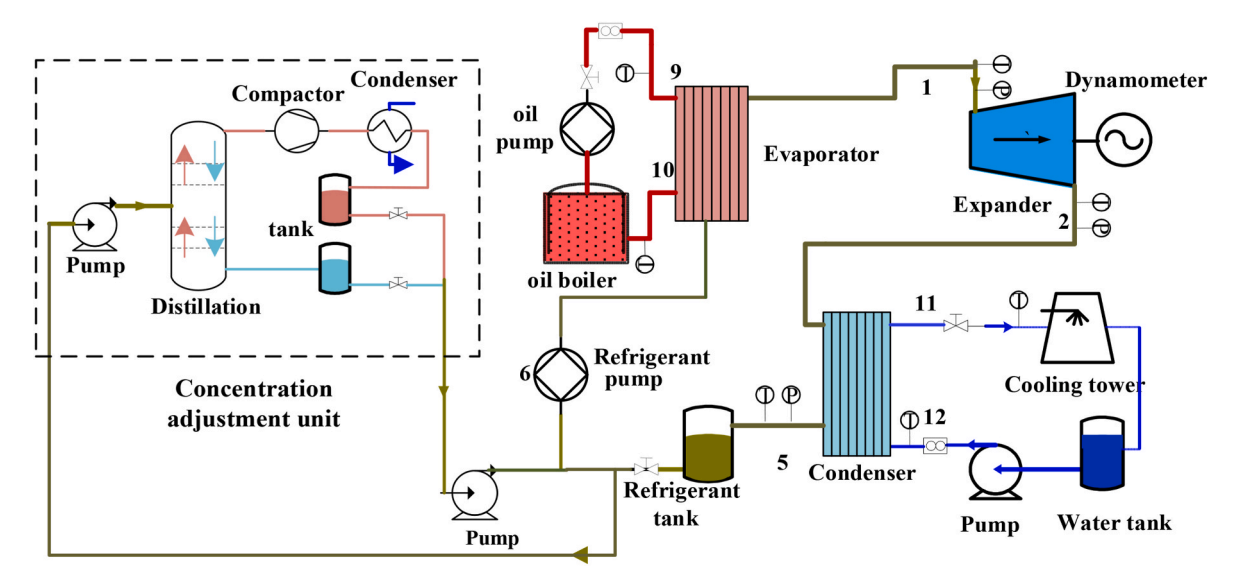


Fig. 1. Schematic diagram of mixture working fluid ORC system.

simple configuration and operational robustness, the organic Rankine cycle (ORC) has gained considerable interest as an effective solution for converting low-grade thermal energy to power [3]. It has demonstrated strong potential applications in various fields such as the recovery of industrial waste heat [4], solar-driven thermal energy conversion [5], geothermal power [6], and electricity generation from biomass combustion [7]. Researchers have extensively explored this technique in recent years, focusing on system analysis [8,9], working fluid screening [10,11], and cycle configuration improvement [12,13].

Utilizing the mixture working fluid in the ORC leads to a temperature glide during phase change, which enhances the thermal matching within heat exchangers such as the condenser and evaporator, thereby reducing thermal exergy losses and enhancing the system performance [14]. Many scholars have conducted experimental studies and thermodynamic analysis on mixture working fluid ORC [15,16]. Li et al. [17] observed a 4.45 % thermal efficiency with R245fa/R601a(0.72:0.28), exceeding pure R245fa (4.38 %). Yang et al. [18] found that an ORC system using R1234ZEZ/R1233ZDE (25/75 wt%) achieved 19.96 % higher power output than pure R1234ZEZ and 18.65 % higher than R1233ZDE. Liu et al. [19] constructed a thermodynamic model of a geothermal-driven cogeneration system containing DORC using a mixture working fluid. The mixture of butene/isopentane with a mass fraction of 0.442:0.558 delivers the best performance. The study results of Xia et al. [20] show that compared to pure working fluids, mixture working fluids significantly enhance the thermodynamic and economic performance of ORC-VCR systems by better matching temperatures during phase change. In the work of Feng et al. [21], ORC systems using mixture working fluids lead to improved thermodynamic efficiency and greater economic advantages compared to pure fluids. In addition, the use of zeotropic mixtures in supercritical ORC systems has also been demonstrated to improve system performance compared to pure working fluids [22,23].

In ORC systems using a mixture working fluid, the optimal mixture concentration that maximizes thermal efficiency is primarily influenced by the heat source temperature [24,25]. Pang et al. [26] evaluated an ORC using R245fa, R123, and their mixtures at heat source temperatures of 120 °C and 110 °C. At 120 °C, the R245fa/R123 (2:1) produces the highest net power output, while at 110 °C, pure R245fa performs best. Braimakis et al. [5] analyzed ORC systems using mixtures of R32 and eight ultra-low GWP fluids. The optimal concentration of R32/R1234ZE is 0.8/0.2 at the heat source temperature of 120 °C, and 0.9/0.1 at 160 °C. Bamorovat et al. [27] analyzed ORC using a 0.6 R245fa/0.4 R134a mixture over heat source temperatures from 80 °C to 120 °C. The

mixture outperforms pure fluids at 100 $^{\circ}\text{C},$ while pure R245fa yields higher power output at 120 $^{\circ}\text{C}.$

The aforementioned studies highlight the thermodynamic advantages of using zeotropic mixtures in ORC systems under idealized steadystate or design conditions. However, practical applications often involve fluctuations in the heat source/sink, such as the geothermal water, solar energy, and the environmental temperature. As the above literature indicates that the optimal composition of the mixture working fluid is sensitive to heat source temperature, this inspires that the mixture concentration could also be a control variable to make the ORC system more adaptive to the fluctuating heat source/sink and enhance the system performance. Wang et al. [28] used R245fa/R134a in an ORC system coupled with a vapor compression refrigeration cycle, demonstrating improved dynamic adaptability to variations in mass flow rate and heat source temperature. Chen et al. [29] conducted a dynamic modeling of ORC systems utilizing zeotropic mixtures under heat source temperature fluctuations, subsequently developing three control strategies to enhance the system performance. Lu et al. [30] introduced an ORC system employing a liquid-separation condenser to adjust the mixture composition. The ORC system achieves a 0.52 % increase in annual net power generation, a 2.20 % enhancement in average thermal efficiency. Liu et al. [31] compared three ORC systems and found that the composition-adjustable ORC achieved 2.4 %-5.3 % higher net output than the basic ORC under off-design conditions. Collings et al. [32] proposed a dynamic modelling of an ORC with a binary zeotropic mixture, in which the fluid composition is regulated in response to variations in ambient temperature. The thermal efficiency and economic performance are improved. In the study of Wang et al. [33], a real-time control strategy for regulating the composition of zeotropic working fluids in an ORC system based on ambient temperature was proposed. This approach improved geothermal power generation efficiency.

The literature review above demonstrates the thermodynamic benefits of zeotropic mixtures. For the regulation of mixture concentration in the ORC system, some scientific gaps remain. Most studies rely on steady-state thermodynamic analysis or simulation, and the dynamic ORC models still need to be developed and shed light on the transient operation characteristics and the effect of concentration regulation on the system control and performance. Besides, current control strategies predominantly target single objectives. The mixture concentration and the mixture mass flow rate could both be the control variables. Whether the dual-objective control of the ORC could be realized and its dynamic behaviors and performance need to be explored.

This work developed a dynamic ORC model based on a 4-kW ORC

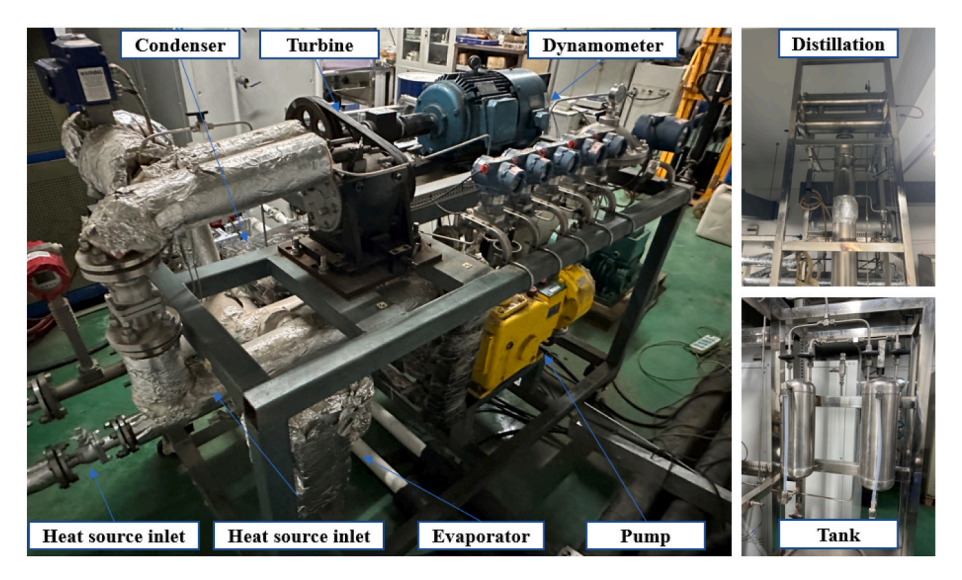


Fig. 2. The prototype of mixture working fluid ORC.

Table 1 Components of the ORC system.

Components	Туре	Capacity/Range	Precision
Boiler	electric	100 kW	±1 °C
Cooling tower	closed-loop	152 kW	_
Expander	scroll	4 kW	_
Evaporator	plate heat exchanger	5.7 m^2	_
condenser	plate heat exchanger	4.6 m ²	_
pump	diaphragm pump	2500 kg/h	_
Distillation	Intermittent	5 L/event	_
Temperature sensor	T-type thermocouple	−200-350 °C	±0.5 °C
Pressure sensor	Capacitive	0-3 MPa	± 0.1 % F.S
Rotational sensor	Rotating speed	0-6000 rev/min	1.0 rev/min
	Shaft torque	0–100 Nm	0.5 % F.S

Table 2 Error analysis of the key parameters.

Parameter	Related variables	Relative uncertainty
Enthalpy, h	T, P	0.5 % (vapor)
		0.3 % (liquid)
Heat transfer rate, Q	m, h	1 %
Measured shaft power, $W_{t,m}$	N_t , T_t	0.5 %
Measured thermal efficiency, η_m	$W_{t,m}, Q$	1.1 %

prototype employing mixture working fluids. The impact of mixture concentrations on ORC performance was analyzed. Two dual-objective control strategies were proposed and simulated: constant output power operation and constant evaporation pressure operation using PI control to adjust the concentration and mass flow rate of the mixture working fluid. A comparative analysis with the basic ORC using pure working fluid and ORC with fixed-concentration mixture is also performed to investigate the system behavior and performance with mixture concentration regulation. Innovations of this work: (1) The regulation of mixture concentration is proposed as a control approach to enhance the adaptability of the ORC to fluctuating heat source/sink. (2) The dual-objective control of the ORC is realized by the coordinated adjustment of mixture concentration and mass flow. (3) The system control range and performance are both improved under the constantevaporation-pressure and constant-output-power operations compared to the BORC and MORC.

2. ORC system and component model

This section introduces the tested ORC prototype in the lab, the developed transient model of the ORC components and system, and the model validation based on the experimental results.

2.1. The ORC system

Fig. 1 illustrates the schematic layout of the concentration-adjustable ORC system using mixture working fluid. Fig. 2 shows the ORC prototype built in the lab, comprising five integrated subsystems: an electric boiler of conductive oil adopted as the heat source, a closed-loop cooling tower used as the cooling source, an ORC unit featuring a scroll expander and plate heat exchangers, a batch distillation unit for concentration adjustment, and an AC dynamometer unit monitoring and controlling the expander rotating speed, shaft torque and shaft power. Detailed information on the components of the ORC system is given in Table 1. The working fluid is compressed through the pump and heated in the evaporator, expands through the scroll expander to generate power, and then condensed in the condenser. The unique distillation unit enables dynamic concentration adjustment by separating and recombining mixture components in precise ratios.

The temperature, pressure, and mass flow rate of thermal oil, cooling water, and mixture working fluid in each subsystem, along with the expander rotating speed and shaft torque, are monitored and recorded in real-time. As certain parameters need to be derived from the measured temperatures and pressures, their error analysis is conducted using the following general expression:

$$\Delta Y = \sqrt{\sum_{i} \left(\frac{\partial Y}{\partial X_{i}}\right)^{2} \Delta X_{i}^{2}} \tag{1}$$

$$e_Y = \frac{\Delta Y}{Y} \tag{2}$$

where ΔY and e_Y are the uncertainty and relative uncertainty of the variable Y. X_i represents the independent variable in equations. Table 2 presents the error analysis of key parameters, where data with subscript "m" in tables denote measured values.

2.2. The dynamic model

The dynamic models for all components of the ORC prototype are

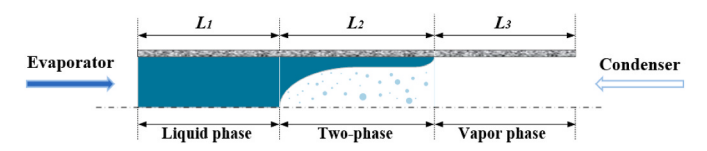


Fig. 3. Illustration of the moving boundary structure of the heat exchanger.

 Table 3

 Heat transfer coefficients in different phase regions.

Heat exchanger segment	Heat transfer coefficient
Evaporator single-phase fluid [35]	$\alpha = 0.2092 \frac{\lambda}{2d_e} \text{Re}^{0.78} (\text{Pr})^{\frac{1}{3}}$
Evaporation process [36]	$c_1 = 2.81 \left(rac{b}{d_e} ight)^{-0.041} \left(rac{\pi}{2-a} ight)^{-2.83}$
	$c_2 = 0.746 \left(\frac{b}{d_e}\right)^{-0.082} \left(\frac{\pi}{2-a}\right)^{-0.61}$
	$lpha = 0.6 rac{\lambda}{d_e} c_1 Re^{c_2} Bo^{0.3} \ ext{Pr}^{0.4}$
The heat source side [37]	$\alpha = 0.724 \frac{\lambda}{d_e} (6 \frac{a}{\pi})^{0.646} \text{Re}^{0.583} (\text{Pr})^{\frac{1}{3}}$
Condenser single-phase fluid [38]	$\alpha = 0.317 \frac{\lambda}{d_e} Re^{0.703} \text{ Pr}^{1/3}$
Condensation process [39]	$\alpha = 4.118 \frac{\lambda}{d_e} \text{Re}^{0.4} \text{Pr}^{1/3}$
The cold source side [40]	$\alpha = 0.2121 \frac{\lambda}{d_e} \text{Re}^{0.78} \text{ Pr}^{1/3}$

developed in the Simulink environment and connected according to the process in Fig. 1 to form the dynamic model of the ORC system.

2.2.1. Modeling of the evaporator and condenser

The moving boundary method is employed to model the heat transfer processes in the evaporator and condenser, which is widely used in dynamic heat exchanger analysis to effectively simulate the movement of the phase change interface [34], as illustrated in Fig. 3. A series of assumptions are introduced to the heat transfer model to ensure computational efficiency while maintaining an accurate representation of physical processes:

- (1) The heat exchanger channels are assumed to facilitate the onedimensional fluid flow.
- (2) The evaporation temperature is assumed to remain unaffected by pressure drops in the system, as this effect is typically minor and can be ignored in preliminary analyses.
- (3) Gravitational effects on heat transfer are assumed to be negligible. In many heat exchanger designs and operating conditions, gravity effects are relatively minor compared to other mechanisms, making this assumption reasonable for simplifying the model.

The heat transfer process in the evaporator is simulated by dividing the working fluid into three phase regions with time-varying boundaries. For each region, the lumped-parameter method is employed to characterize the thermodynamic properties. The mathematical model is developed based on conservation equations [34]:

Mass conservation equation:

$$\frac{\partial \rho}{\partial t} + \frac{\partial (\rho v)}{\partial z} = 0 \tag{3}$$

Energy conservation equation:

$$\frac{\partial(\rho h - p)}{\partial t} + \frac{\partial(\rho v h)}{\partial z} = \frac{4}{d_e} \alpha_i (T_w - T) \tag{4}$$

Leibniz formula [35] equation:

$$\int_{z_{0}}^{z_{2}} \frac{\partial f(z,t)}{\partial t} dz = \frac{d}{dt} \int_{z_{0}}^{z_{2}} f(z,t) dz - f(z_{2},t) \frac{dz_{2}}{dt} + f(z_{1},t) \frac{dz_{1}}{dt}$$
 (5)

The conservation equations for the different phase regions are simplified using the Leibniz formula to obtain the moving boundary model [35].

(1) preheating region

Working fluid mass conservation equation:

$$A\frac{dL_{1}}{dt}\left(\rho_{L}-\rho_{f}\right)+\frac{1}{2}AL_{1}\frac{\partial\rho_{L}}{\partial h_{1}}\Big|_{p}\frac{dh_{in}}{dt}+AL_{1}\left(\frac{1}{2}\frac{\partial\rho_{L}}{\partial h_{1}}\Big|_{p}\frac{dh_{f}}{dp}+\frac{\partial\rho_{L}}{\partial p}\Big|_{h_{1}}\right)\frac{dp}{dt}=m_{in}$$

$$-m_{f}$$
(6)

Working fluid energy conservation equation:

$$\left(\rho_{L}h_{L} - \rho_{f}h_{f}\right) \frac{dL_{1}}{dt} + \frac{1}{2}AL_{1}\left(\rho_{L} + h_{L}\frac{\partial\rho_{L}}{\partial h_{L}}\Big|_{p}\right) \frac{dh_{in}}{dt}$$

$$+ AL_{1}\left[\frac{1}{2}\left(\rho_{L} + h_{L}\frac{\partial\rho_{L}}{\partial h_{L}}\Big|_{p}\right) \frac{dh_{f}}{dp} + h_{L}\frac{\partial\rho_{L}}{\partial p}\Big|_{h_{L}} - 1\right] \frac{dp}{dt}$$

$$+ m_{f}h_{f} - m_{in}h_{in} = \alpha_{e1}(T_{w1} - T_{s})L_{1}$$

$$(7)$$

Tube wall energy conservation equation:

$$c_{\rm w}\rho_{\rm w}d_{\rm w}\frac{dT_{\rm w}}{dt} = \alpha_{\rm ew}(T_{\rm a} - T_{\rm w1}) + \alpha_{\rm e1}(T_{\rm s} - T_{\rm w1})$$
 (8)

(2) two-phase region

Working fluid mass conservation equation:

$$A(\rho_{\rm f} - \rho_{\rm g})\gamma \frac{dL_1}{dt} + A(\rho_{\rm f} - \rho_{\rm g})(1 - \gamma)\frac{dL_2}{dt} + A(L_2 - L_1)\left[(1 - \gamma)\frac{d\rho_{\rm f}}{dp} + \gamma \frac{d\rho_{\rm g}}{dp} \right] \frac{dp}{dt} = m_{\rm f} - m_{\rm g}$$

$$(9)$$

Working fluid energy conservation equation:

$$\begin{split} A(L_{2}-L_{1}) & \left[(1-\gamma) \frac{d\rho_{\rm f} h_{\rm f}}{dp} + \gamma \frac{d\rho_{\rm g} h_{\rm g}}{dp} - 1 \right] \frac{dp}{dt} + \\ \gamma A \left(\rho_{\rm f} h_{\rm f} - \rho_{\rm g} h_{\rm g} \right) \frac{dL_{1}}{dt} + A \left(\rho_{\rm f} h_{\rm f} - \rho_{\rm g} h_{\rm g} \right) (1-\gamma) \frac{dL_{2}}{dt} + \\ m_{\rm g} h_{\rm g} - m_{\rm f} h_{\rm f} & = \alpha_{\rm c2} (T_{\rm w2} - T_{\rm s}) (L_{2} - L_{1}) \end{split} \tag{10}$$

Tube wall energy conservation equation:

$$c_{\rm w}\rho_{\rm w}d_{\rm w}\frac{dT_{\rm w2}}{dt} = \alpha_{\rm ew}(T_{\rm a} - T_{\rm w2}) + \alpha_{\rm e2}(T_{\rm s} - T_{\rm w2}) \tag{11}$$

(3) superheating region

Working fluid mass conservation equation:

$$\frac{1}{2}A(L-L_{2})\frac{\partial\rho_{\nu}}{\partial h_{\nu}}\Big|_{p}\frac{dh_{\text{out}}}{dt} + A(L-L_{2})\left(\frac{\partial\rho_{\nu}}{\partial p}\Big|_{h_{\nu}} + \frac{1}{2}\frac{\partial\rho_{\nu}}{\partial h_{\nu}}\Big|_{p}\frac{dh_{g}}{dp}\right)\frac{dp}{dt} + A\left(\rho_{g} - \rho_{\nu}\right)\frac{dL_{2}}{dt} = m_{g} - m_{\text{out}}$$
(12)

Working fluid energy conservation equation:

$$A(L - L_{2}) \left[h \frac{\partial \rho_{\nu}}{\partial p} \Big|_{h} + \frac{1}{2} \left(\rho_{\nu} + h \frac{\partial \rho_{\nu}}{\partial x h_{\nu}} \Big|_{p} \right) \frac{dh_{g}}{dp} - 1 \right] \frac{dp}{dt} + \frac{1}{2} A(L - L_{2}) \left(\rho_{\nu} + h_{\nu} \frac{\partial \rho_{\nu}}{\partial h_{\nu}} \Big|_{p} \right) \frac{dh_{out}}{dt} + A \left(\rho_{g} h_{g} - \rho_{\nu} h \right) \frac{dL_{2}}{dt} + m_{out} h_{out} - m_{g} h_{\sigma} = \alpha_{e3} (T_{w3} - T_{s}) (L - L_{2})$$

$$(13)$$

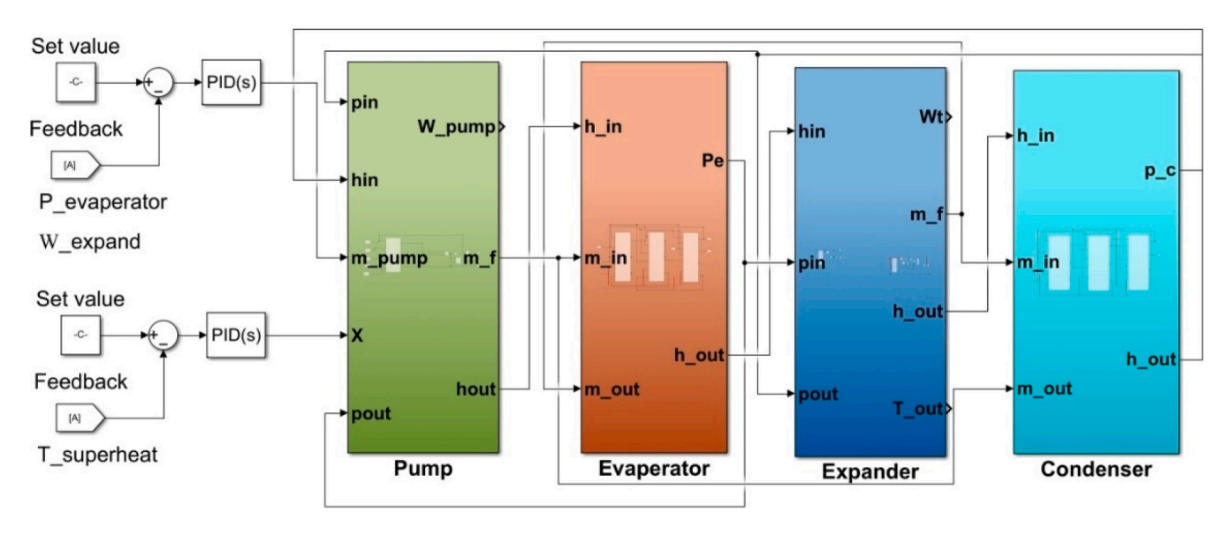


Fig. 4. The ORC dynamic simulation model.

Tube wall energy conservation equation:

$$c_{\rm w}\rho_{\rm w}d_{\rm w}\frac{dT_{\rm w3}}{dt} = \alpha_{\rm ew}(T_{\rm a}-T_{\rm w3}) + \alpha_{\rm e3}(T_{\rm s}-T_{\rm w3}) \tag{14}$$

(4) heat source side

$$T_{\text{out.ei}} = T_{\text{w.ei}} - (T_{\text{in.ei}} - T_{\text{w.ei}})e^{-a}$$
 (15)

$$a = \frac{A_{\rm ei}\alpha_{\rm ew}}{c_{\rm e}m_{\rm e}} \tag{16}$$

The modeling approach for the heat transfer process in the condenser follows a similar formulation to the previously presented equations, with the primary distinction being that the working fluid flows in the opposite direction compared to the evaporator. Table 3 summarizes the heat transfer coefficients of the condenser and evaporator in various phase regions.

2.2.2. The pump model

Because the working fluid flows much faster through the expander and pump than through the heat exchangers, steady-state modeling is applied to these two components. The pump raises the fluid pressure to ensure effective circulation throughout the system. The calculation of pump power consumption is given by:

$$W_{\rm p} = \frac{W_{\rm p.s}}{\eta_{\rm p}} = m_{\rm p} \frac{(h_{\rm 6s} - h_{\rm 5})}{\eta_{\rm p}} = m_{\rm p} (h_{\rm 6} - h_{\rm 5}) \tag{17}$$

$$\eta_{\rm p} = \eta_{\rm p,d} \left(\frac{m_{\rm p}}{m_{\rm d}}\right)^n \tag{18}$$

where $\eta_{\rm p,d}$ denotes the isentropic efficiency of the pump. The values of $\eta_{\rm p,d}$, $m_{\rm d}$, and n are 0.84, 2500 kg/h, and 0.34, determined based on the performance characteristics of the diaphragm pump employed in this study.

2.2.3. The expander model

The expander serves as the key energy conversion component in the ORC system. The working fluid undergoes three sequential processes in the expander:

First, the vapor is drawn into the scroll chamber from the pipeline during the suction process. The power during the suction process is [41]:

$$w_{\rm in} = h_{\rm in} - u_{\rm in} = p_{\rm in} v_{\rm in} \tag{19}$$

Next, an expansion occurs within the expansion chamber. The rotation of the scrolls is driven by vapor expansion within the chamber.

This process is assumed to be reversible and adiabatic. The expansion work is:

$$w_{s} = u_{in} - u_{c} = h_{in} - p_{in}v_{in} - (h_{c} - p_{c}v_{c})$$
(20)

Finally, the vapor is discharged into the exhaust pipeline. The work consumption is given by:

$$w_{\rm ex} = p_{\rm d} v_{\rm c} \tag{21}$$

Under-expansion or over-expansion in the expander results from deviations in the operating pressure ratio from the design value [42], leading to the loss of power. The actual output power is:

$$w_{\rm exp} = \eta_{\rm exp}(w_{\rm in} + w_{\rm s} - w_{\rm ex}) = \eta_{\rm exp}[h_{\rm in} - h_{\rm c} + v_{\rm c}(p_{\rm c} - p_{\rm d})]$$
 (22)

where $\eta_{\rm exp}$ is assumed to be 0.63 [43], reflecting the combined efficiency of the expander considering the previously discussed effects.

The vapor mass flow rate through the expander is determined by the following equation:

$$m_{\rm exp} = \frac{\rho_{\rm i} N_{\rm exp} V}{60} \tag{23}$$

where $N_{\rm exp}$ denotes the expander rotating speed, and V represents the swept volume.

The net output power is determined by the following equation:

$$W_{\text{net}} = W_{\text{exp}} - W_{\text{p}} = w_{\text{exp}} m_{\text{exp}} - W_{\text{p}} \tag{24}$$

Consequently, exergy and thermal efficiencies are calculated using the following equations:

$$\eta_{\text{thermal}} = \frac{W_{\text{net}}}{m_{\text{exp}}(h_1 - h_5)} \tag{25}$$

$$\eta_{\text{exergy}} = \frac{W_{\text{net}}}{m_{\text{hr}}[(h_9 - h_{10}) - T_0(s_9 - s_{10})]}$$
 (26)

where T_0 corresponds to the ambient temperature, serving as the reference state.

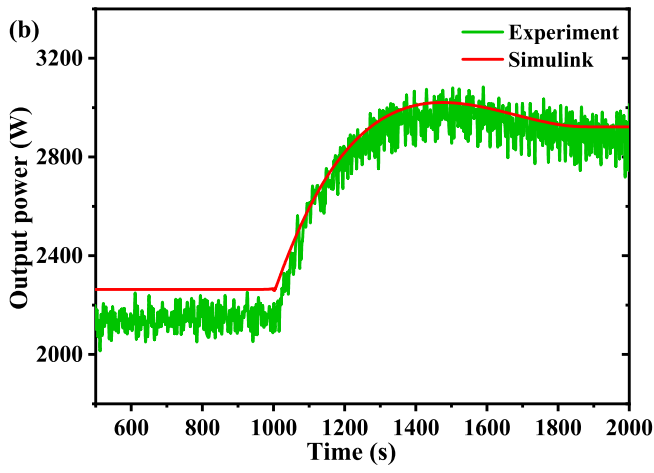
2.2.4. System model

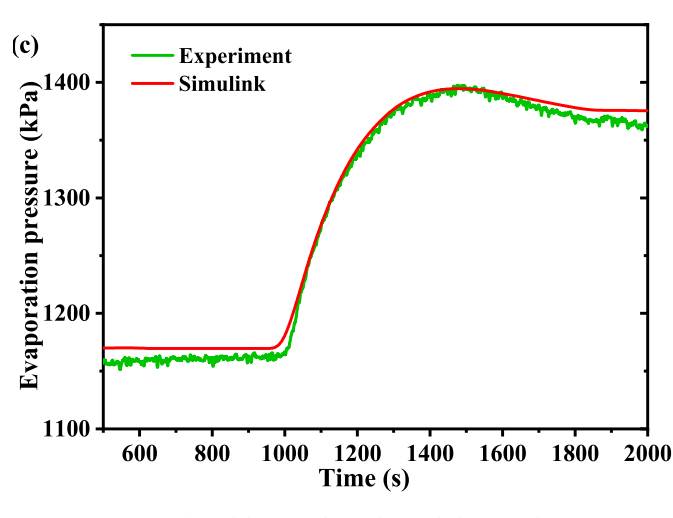
Utilizing the aforementioned component models and the intercomponent coupling relationships, the dynamic simulation model of the ORC system was implemented in the Simulink environment. Fig. 4 presents the ORC system model, which comprises four main components: pump, expander, condenser, and evaporator. The model incorporates dual PID controllers for system regulation: a concentration controller that adjusts the concentration of the mixture circulating in the

Table 4 Verification of working conditions.

Parameters	Value
$T_{ m hf}$	120 °C–130 °C
$V_{ m hf}$	8800 L/h
$T_{\rm cool}$	15 °C
$V_{ m cool}$	3100 L/h
Working fluid	0.25R236fa/0.75R123
M_{wf}	700 kg/h
$N_{\rm exp}$	1600 rev/min
$N_{\rm exp}$	1600 rev/min

(a) 135 — Experiment — Simulink —





ORC loop according to real-time thermal feedback (typically the vapor superheat), and a mass flow rate controller that maintains optimal superheat by regulating the mixture mass flow rate based on deviations between measured evaporator pressure or system power.

The inter-component coupling relationships are as follows: the pump module, according to the working fluid initial state parameters (including key variables such as inlet enthalpy and mass flow rate), performs compression calculations and transmits the working fluid state parameters to the evaporator module. The evaporator model accurately simulates the multi-stage heat transfer process from liquid preheating,

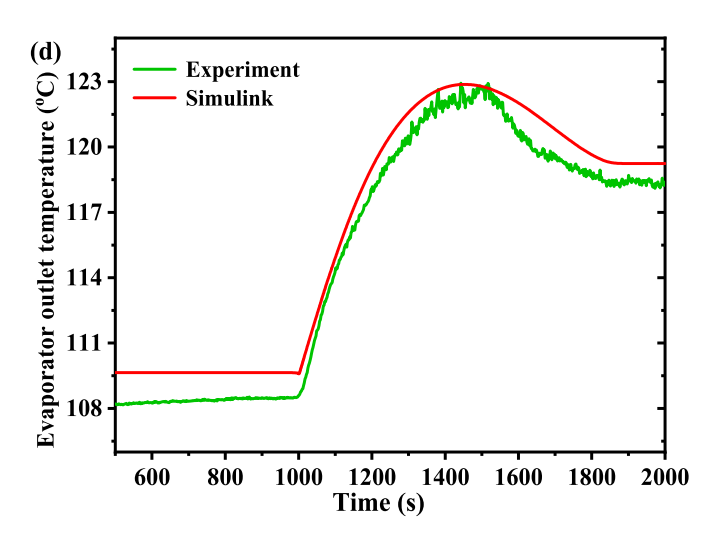


Fig. 5. Comparison of modeling results and tested data: (a) heat source temperature, (b) output power, (c) evaporation pressure, and (d) evaporator outlet temperature.

Table 5The main operating parameters of the ORC system.

Parameters	Value
$T_{ m hf}$ $V_{ m hf}$ $T_{ m cool}$ $V_{ m cool}$ $M_{ m wf}$ Working fluid	120 °C 3000 L/h 20 °C 3100 L/h 750 kg/h R236fa/R123
$N_{ m exp}$	1600 RPM

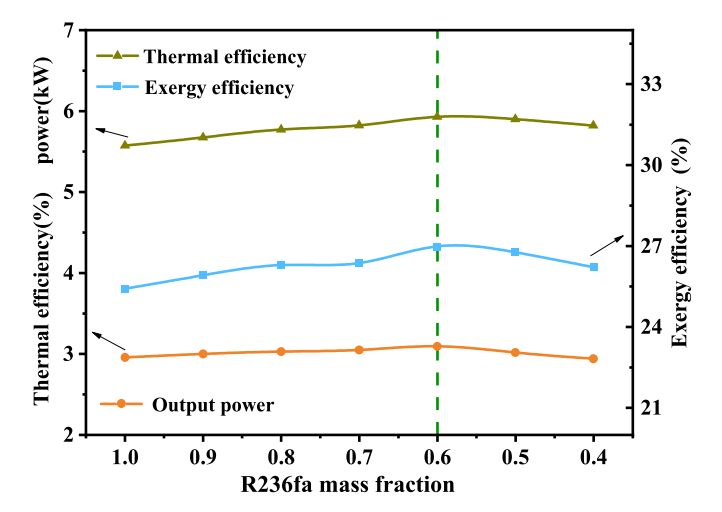


Fig. 6. Variation of output power and efficiencies with R236fa mass fraction.

phase-change heat absorption to superheated vapor generation. The calculated evaporator outlet parameters are then input as boundary conditions to the expander model to calculate the expansion work. Finally, the expander exhaust parameters are fed into the condenser module to simulate the heat rejection and phase-change processes, thereby completing the system-level simulation across one time step.

This dynamic simulation includes the independent operating characteristics of each component and integrates the interactions and influences between them, so as to more accurately represent the system's performance under varying operating conditions, including changes in parameters such as mass flow rate, temperature, and pressure. Additionally, the model serves as a tool to evaluate and validate the impact of various control strategies on ORC system performance, which is critical for the development of an efficient and reliable system.

2.3. Model validation

To validate the accuracy of the model, simulations were conducted under identical conditions to those used in the experiments, as given in Table 4. Experimental data corresponding to a heat source temperature ($T_{\rm hf}$) varying between 120 °C and 130 °C are selected for comparison with the simulation results.

The variation of the conductive oil temperature during the test and simulation is shown in Fig. 5(a), while the other parameters are kept consistent. Fig. 5(b–d) compares the experimental data and simulation results of the output power, evaporator outlet temperature, and evaporation pressure. The relative errors are about 2 %, 0.9 % and 1 % for these three parameters, respectively.

3. Results and discussion

This section explores the specific impacts and underlying mechanisms by which concentration adjustments of the mixture working fluid influence the system performance. Based on its dynamic characteristics,

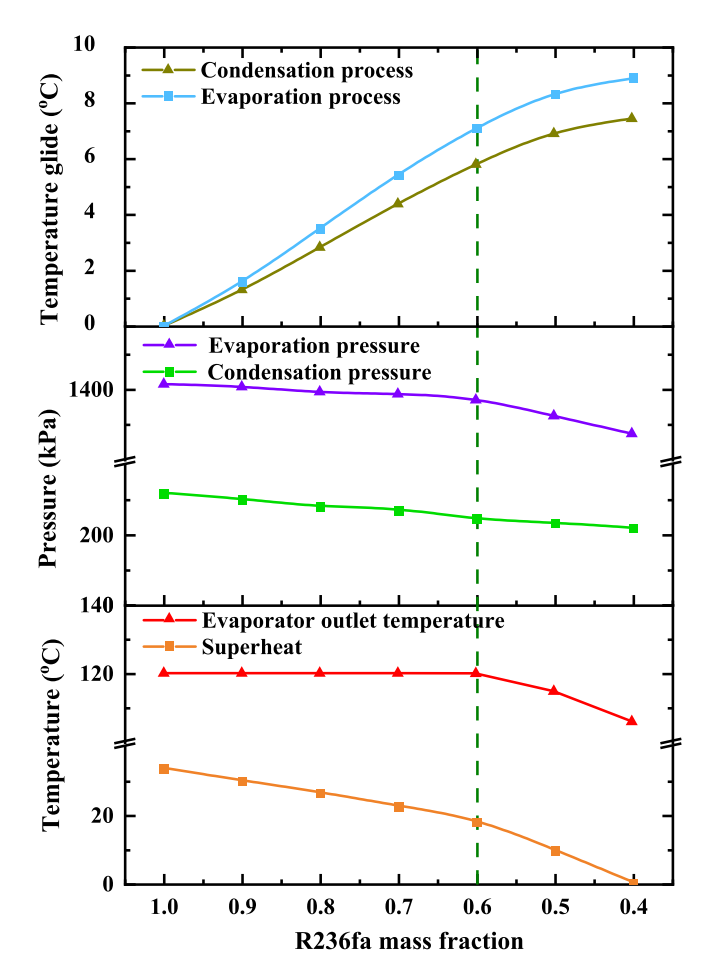


Fig. 7. Variation of key system parameters with R236fa mass fraction.

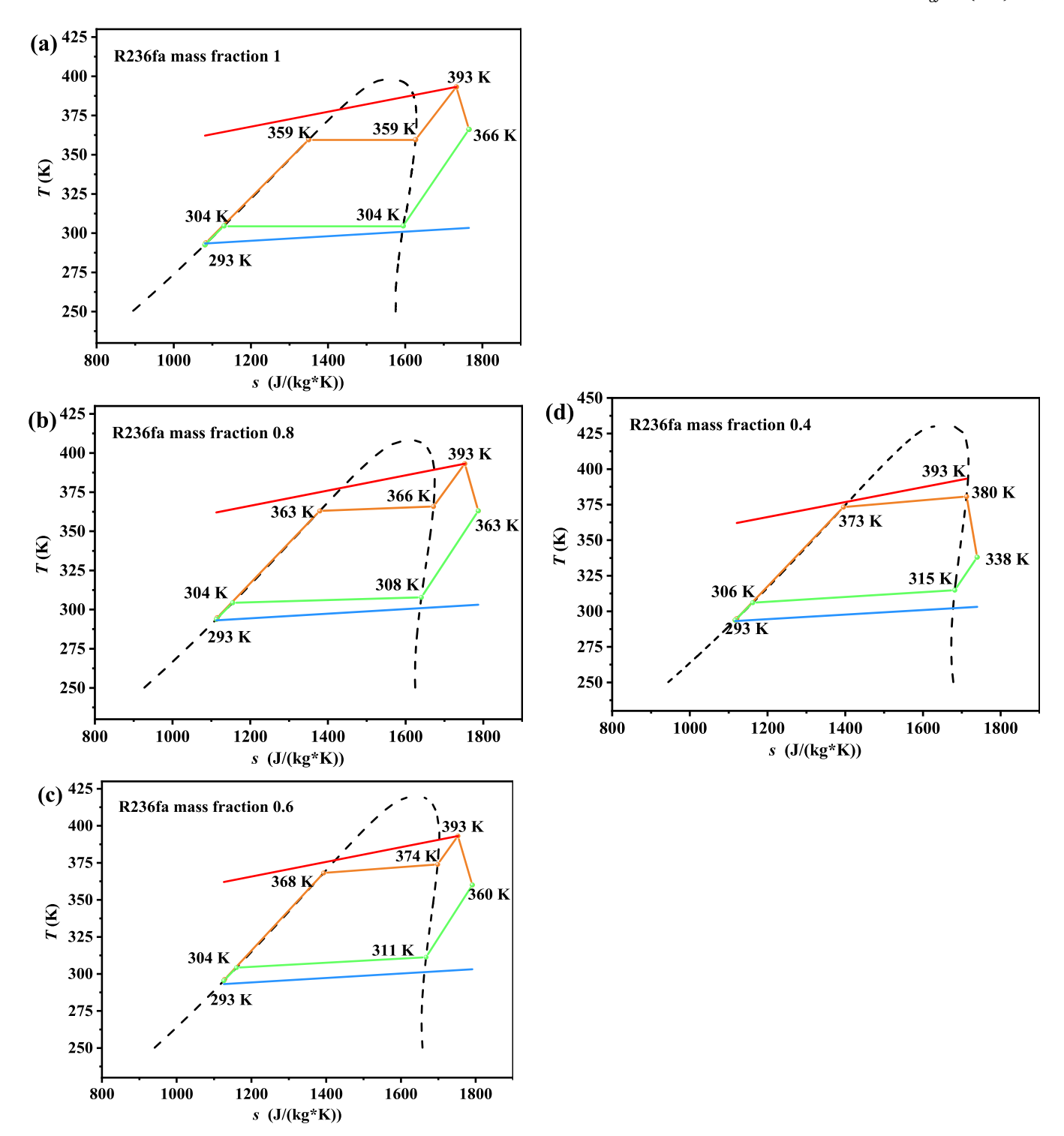
two control strategies are proposed: constant evaporation pressure (CP) and constant output power (CW).

3.1. Influence of mixture working fluid on system performance

The same working fluids as the experiments in Section 2: R236fa, R123, and their mixtures, are selected for the simulation in this section. To facilitate the comparison of the effects of different mass fractions of species on the system performance, the basic simulation conditions are set, details of which are given in Table 5. According to the results obtained from the preceding experiments, if the $T_{\rm hf}$ is too high, a large redundancy of the heat exchange area of the evaporator occurs, which makes the outlet temperature of the working fluid from the evaporator closely match the $T_{\rm hf}$ and is unfavorable for the analysis of the heat exchange efficiency. Therefore, $T_{\rm hf}$ is set to 120 °C. Other external conditions are kept constant in the simulation process, and only the mixture mass fraction is adjusted to analyze the changes in system performance.

Fig. 6 illustrates the variation of exergy efficiency, thermal efficiency, and output power of the ORC system concerning the mass fraction of R236fa. It can be observed that the system output power initially increases and subsequently decreases as the mass fraction of R236fa decreases. Thermal and exergy efficiencies exhibit a similar trend. The performance of the system reaches its peak when the mass fraction of R236fa is 0.6, with the output power increasing by 140 W (approximately 5 %) compared to the use of pure R236fa. Additionally, the thermal efficiency increases from 5.57 % to 5.92 %, while the exergy efficiency improves from 25.4 % to 26.97 %.

Fig. 7 illustrates the variation of key operating parameters of the



 $\textbf{Fig. 8.} \ \textit{T-} s \ diagrams \ for \ different \ mixture \ compositions.$

ORC system with the R236fa mass fraction. As the mass fraction of R236fa decreases from 1.0 to 0.4, the temperature glide during the phase change process gradually increases. The condenser exhibits a greater temperature glide compared to the evaporator. Compared to the cooling source, considering the substantially larger temperature fluctuations of the heat source, the use of a mixture working fluid mainly serves to improve the temperature match between the cooling source and the working fluid in the condenser. As the mass fraction of R236fa decreases, the condensation pressure, evaporation pressure, and vapor superheat progressively decline. The evaporation pressure was reduced

by 140 kPa, about 10 %, while the condensation pressure was reduced by 100 kPa, about 28 %, with the mass fraction of R236fa decreasing from 1.0 to 0.4. At the same time, the vapor superheat decreases from 34 °C to nearly 0 °C, which limits the simulation to a minimum R236fa mass fraction of 0.4 to prevent liquid entrainment at the expander inlet. In addition, the evaporator outlet temperature was maintained at about 120 °C, close to the $T_{\rm hf}$ when the R236fa mass fraction is between 1 and 0.6, whereas it decreases significantly when the mass fraction decreases from 0.6 to 0.4.

From the above analysis, it was found that changes in the mixture

Table 6Key parameters used in the control strategy.

	07	
Control strategy	Working fluid	Abbreviation
Constant output power	R236fa	CW_{BORC}
operation	0.5R236f/0.5R123	CW_{MORC}
	R236f/R123 (concentration	CW_{CAORC}
	adjustable)	
Constant evaporation pressure	R236fa	CP_{BORC}
operation	0.5R236f/0.5R123	CP_{MORC}
	R236f/R123 (concentration	CP_{CAORC}
	adjustable)	
Constant vapor superheat	R236fa	$T_{\text{sup}} = 10 ^{\circ}\text{C}$
operation	0.5R236f/0.5R123	•
	R236f/R123 (concentration	
	adjustable)	

Table 7Parameters used in the dynamic modelling and the distillation process.

Parameters	Value
R236fa/R123	0.2/0.8–1/0
$T_{ m hf}$	100–130 °C (sinusoidal)
$V_{ m hf}$	2000-4000 L/h (sinusoidal)
$T_{\rm cool}$	10–30 °C
Tover	10 °C
$M_{ m wf}$	dependent
$N_{ m exp}$	1600 RPM
Distillation section flow rate	140 kg/h
Distillation pressure	200 kPa
Heat of evaporation	16.22 kJ/kg
Output power	3000 W

concentration have a significant impact on the system key parameters, which is mainly attributed to the effect of phase equilibrium property, that is, the saturation temperature-pressure relation with the mixture concentration. Fig. 8 shows the *T-s* diagram of the ORC system with different R236fa mass fractions to further investigate the intrinsic mechanism by which changes in the concentration regulation of the mixture affect system parameters, as well as the impact of temperature glide on temperature match during the phase change process. In the evaporator, the most volatile component in the mixture evaporates first, leading to a gradual increase in the average boiling point of the mixture during the evaporation process. Conversely, in the condenser, the least condensable component condenses last, resulting in the average condensation temperature of the mixture decreasing progressively

during the condensation process. Both the temperature glide in the condenser and evaporator can optimize the temperature match during heat transfer. At the same time, the more significant effect of the mixture concentration is the variation of the average evaporation and condensation temperature. It can be observed that, with a fixed mass flow rate of the mixture working fluid and a constant expander rotating speed, the average evaporation and condensation temperatures increase as the R236fa mass fraction decreases. Consequently, the temperature difference between the mixture and the heat source becomes smaller, reducing the irreversible losses in the evaporator. However, the temperature difference between the mixture and the cooling source becomes larger simultaneously, which increases the irreversible losses in the condenser. The combined effect results in the highest thermal and exergy efficiencies and maximizes the power output at the R236fa mass fraction of 0.6.

In addition, the comparison of the cycle parameters for the four groups of mixture composition shows that the evaporator outlet superheat decreases as the mass fraction of R236fa decreases. At the end of evaporation, the mixture temperature is close to $T_{\rm hf}$. The reduced heat transfer temperature difference during evaporation of the mixture requires a larger two-phase area, resulting in a smaller superheated area and a smaller vapor superheat.

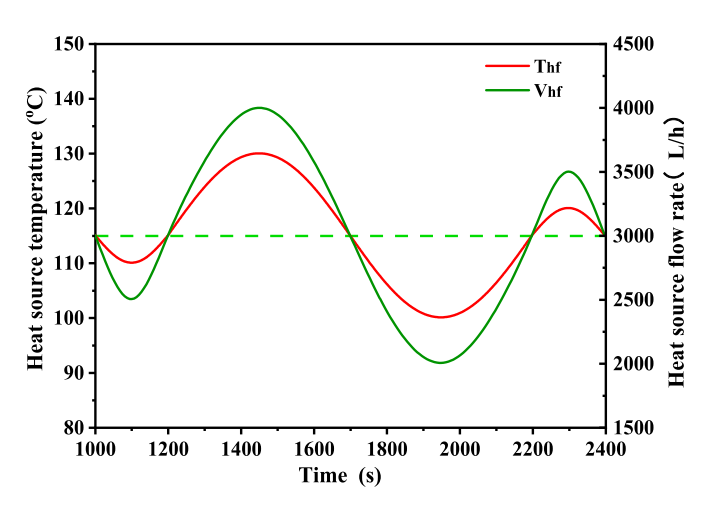


Fig. 10. Variation of heat source temperature with time.

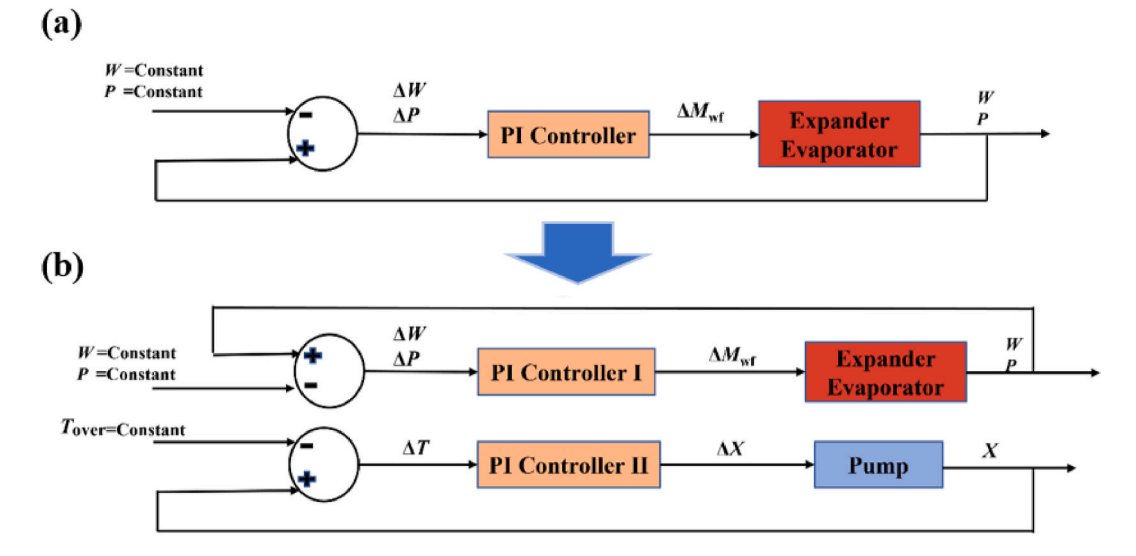


Fig. 9. Control strategy diagram: (a) univariate control of the BORC with pure R236fa and MORC with 0.5R236f/0.5R123, and (b) bivariate control of the CAORC with R236f/R123.

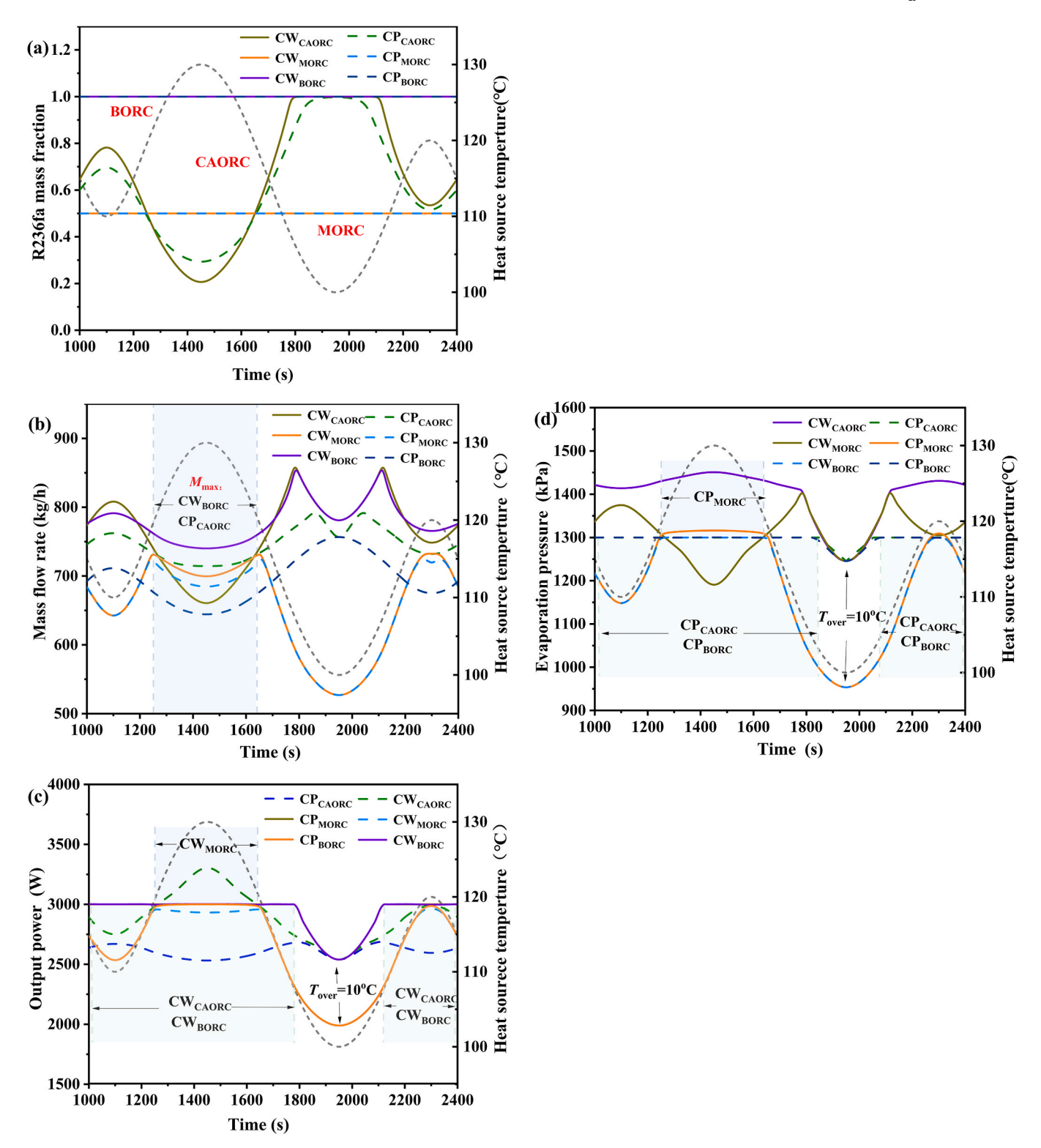


Fig. 11. Variation of control variables and objectives with time under the heat source temperature fluctuation.

3.2. Influence of the mixture concentration regulation on the ORC control strategy

As demonstrated by the results in the preceding section, the temperature of the hot and cold sources can be better matched by adjusting the concentration of the mixture working fluid, thus improving the output power, exergy efficiency, and thermal efficiency. Meanwhile, the change in the mixture concentration also has a significant effect on the

saturation pressures and vapor superheat of the ORC working fluid. This characteristic can help to explore the new control strategy of the ORC operation. At present, the control of the ORC system generally lies in adjusting the speed of the expander and the mass flow rate of the working fluid. However, the frequency of the output power will also fluctuate due to the real-time adjustment of the expander speed. The regulation of mixture concentration will not affect the frequency and can be used as a new ORC control strategy to adapt the ORC operation to

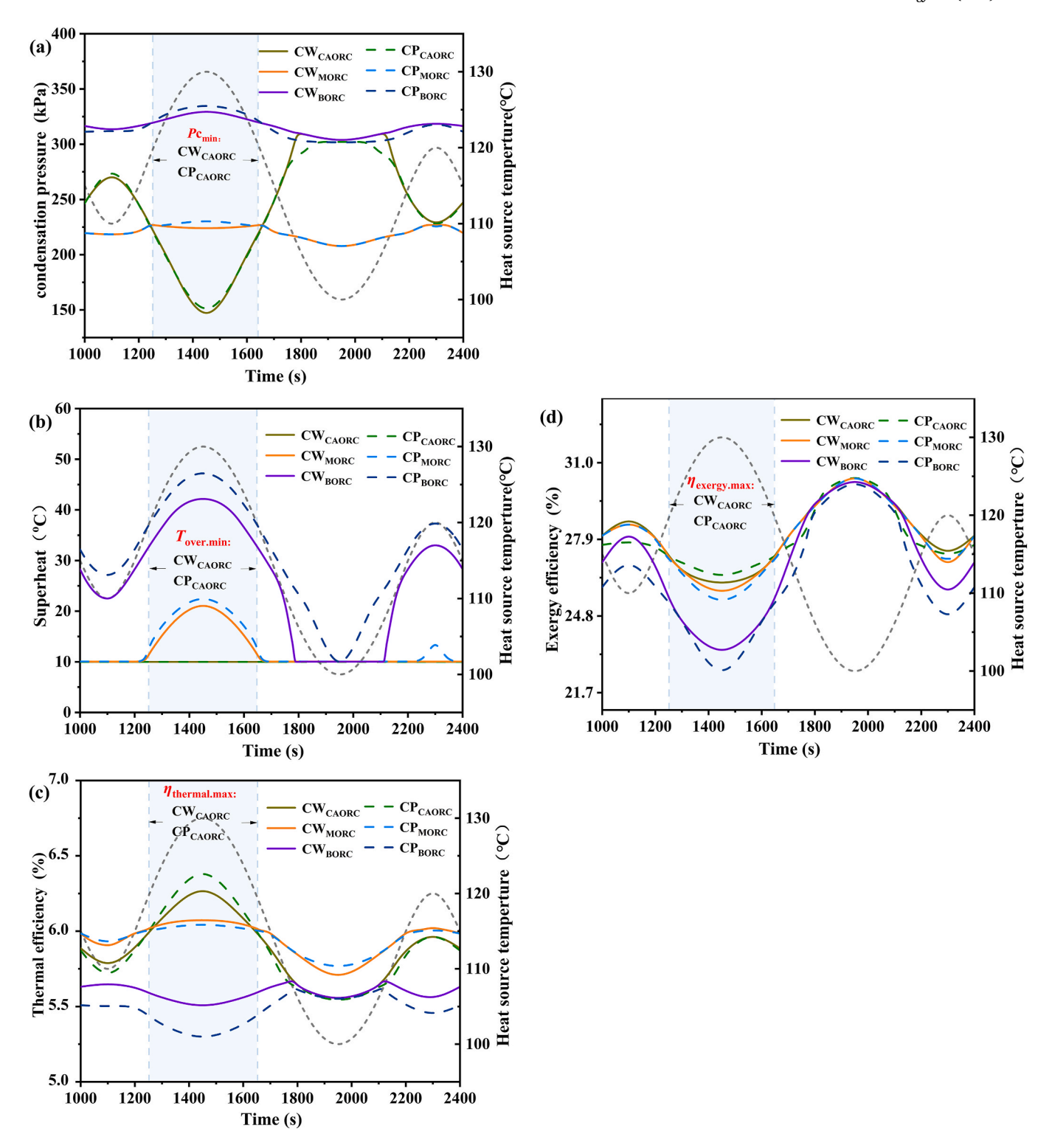


Fig. 12. Temporal variation of key parameters and system performance under the heat source temperature fluctuation.

fluctuations in boundary conditions. The fluctuations of specific boundary condition parameters are presented in Table 7.

The adjustment of the working fluid flow rate is flexible and simple to implement, but it has certain limitations if only this approach is used. When the system operates under CW or CP mode, significant fluctuations in vapor superheat may occur during the control process. Excessively high or low superheat not only reduces the system's thermal efficiency but also poses risks to its safe operation. As discussed in Section 3.1, the vapor superheat is highly sensitive to variations in the

mixture concentration. Therefore, it is possible to regulate the mixture concentration to maintain a constant vapor superheat. In this section, the ORC system is studied by regulating the mixture concentration under CW and CP operating conditions, ensuring that the vapor superheat remains around 10 $^{\circ}\text{C}$ during operation. When the heat source parameters are too low to support either of these two operating modes, the constant vapor superheat operation mode is activated to ensure the system continuous and safe operation. Furthermore, two types of working fluids are selected for comparison: a pure working fluid

Table 8The control range and performance of different operation modes under heat source temperature fluctuations.

Operation mode	Control range	Average thermal efficiency (under shared control range with MORC)	Average exergy efficiency (under shared control range with MORC)
CW _{BORC}	1000–1777 s and 2123–2400 s	5.61 %(5.55 %)	26.61 %(24.4 %)
CW_{MORC}	1255–1645 s	6.04 %	26.44 %
CW _{CAORC}	1000–1777 s and 2123–2400 s	5.91 %(6.11 %)	27.82 %(26.62 %)
CP_{BORC}	1000–1847 s and 2053–2400 s	5.51 %(5.37 %)	26.50 %(24.21 %)
CP_{MORC}	1243–1657s	6.01 %	26.62 %
CP _{CAORC}	1000–1847 s and 2053–2400 s	5.87 %(6.17 %)	27.90 %(26.86 %)

(BORC), R236fa, and a fixed concentration mixture working fluid (MORC): 0.5 R236fa/0.5 R123, as shown in Table 6.

In the system simulation, the ORC system with pure R236fa and fixed-concentration mixture 0.5R236f/0.5R123 adopts univariate control to maintain CW or CP by adjusting the mass flow rate of the working fluid, as shown in Fig. 9 (a). For the CAORC with mixture R236f/R123, bivariate control is applied to regulate both the mass flow rate and the mixture concentration to maintain the two objectives: vapor superheat at $10\,^{\circ}\text{C}$ and constant output power (or constant evaporation pressure), as depicted in Fig. 9 (b).

In addition, the introduction of a concentration regulation unit will increase the system cost, and the distillation process requires additional heat supply. Therefore, it is necessary to analyze its economic feasibility. The heat required during the distillation process can be calculated as:

$$Q_{\min} = Fr\left(\frac{1}{\alpha - 1} + x_{\text{Fa}}\right) \tag{27}$$

where F refers to the feed flow rate, r is the heat of evaporation, $x_{\rm Fa}$ is the lighter composition fraction, while α indicates the relative volatility, defined as the vapor pressure ratio of the two compositions. As an example of concentration regulation when $T_{\rm hf}$ changes, the heat consumed in the distillation process is calculated by selecting the working condition with the most drastic concentration adjustment in the simulation process. Table 7 shows the main parameters of the selected condition. The mixture concentration is changed from 0.5/0.5 to 0.4/0.6 from 1250 s to 1300 s.

During the distillation, the two separated components are stored in independent tanks. To adjust the mixture concentration, the required component is extracted from the storage tank and introduced into the ORC reservoir. As shown in Table 7, only 140 kg/h of the mixture working fluid needs to be extracted for distillation in this case. By adding an equal mass flow rate of R123 to the ORC system, the mixture concentration can be adjusted to 0.4/0.6. The average heat required for the distillation process is 6.3 W, while the ORC output power is 3000 W. The heat required for distillation accounts for only 0.2 % of the system output power. Thus, from the overall system perspective, the heat demand of the concentration regulation unit is insignificant.

3.2.1. Performance of the ORC with heat source temperature fluctuations To investigate the general behavior of the ORC system under fluc-

tuating heat source parameters, this study assumes that the transient $T_{\rm hf}$ and heat source flow rate ($V_{\rm hf}$) follow a series of sinusoidal functions. The variations in $T_{\rm hf}$ and $V_{\rm hf}$ can be represented as time-dependent or aperiodic signals, which are amenable to decomposition into multiple sinusoidal elements of differing frequencies through Fourier transform

techniques. [44,45]. Therefore, to simplify the calculation, $T_{\rm hf}$ and $V_{\rm hf}$ are set to sinusoidal curves varying from 100 °C to 130 °C and from 2000 L/h to 4000 L/h, respectively, as illustrated in Fig. 10. Other parameters of the heat source remain the same as in Section 3.1.

Fig. 11 shows the variation of control variables and objectives over time, where the gray dashed line represents the fluctuations in $T_{\rm hf}$ with time. As shown in Fig. 11(a–b), the mass fraction of R236fa in the ORC system (CW_{CAORC}) fluctuates significantly between 0.2 and 1.0, demonstrating the system rapid response capability under varying operating conditions. In contrast, the mass fraction of R236fa in the BORC and the MORC (0.5R236f/0.5R123) remains stable at 1.0 and 0.5. Under both operational strategies, the working fluid mass flow rates in all three ORC systems exhibit notable fluctuations. The maximum mass flow rates in CW_{BORC} and CW_{CAORC} modes reach 860.94 kg/h and 860.87 kg/h, respectively.

Fig. 11(c-d) compares the control effectiveness of ORC systems under CW and CP modes. In the CW operation, the CAORC and BORC share the same control range. When the $T_{\rm hf}$ lies between 107 $^{\circ}{\rm C}$ and $130\,^{\circ}$ C (1000-1777 s and 2123-2400 s), the systems effectively sustain a stable output power of 3000 W. Their effective control range covers 78.6 % of the fluctuation period of $T_{\rm hf}$. As $T_{\rm hf}$ gradually decreases from 130 °C to 105 °C, the R236fa mass fraction in the CAORC under CW mode gradually increases to 1.0, which is the pure R236fa. When $T_{\rm hf}$ further declines below 107 °C (1777-2123 s), the ORC systems fail to sustain the target output power and switch to a constant superheat mode to maintain a stable superheat of 10 °C, resulting in a decrease in power output. The CAORC matches that of the BORC in the CW mode, leading to similar mass flow rates that fluctuate with $T_{\rm hf}$ until temperatures recover to the controllable range of the CAORC. Comparatively, MORC exhibits the narrowest control range, maintaining constant power output only when $T_{\rm hf}$ is between 120 °C and 130 °C (1250–1650 s), covering merely 28.6 % of the fluctuation period of $T_{\rm hf}$. Outside this range, MORC mode switches to constant superheat mode, where the evaporation pressure varies dynamically with $T_{\rm hf}$, causing output power to drop to a minimum of 2539 W at 100 °C.

The ORC systems operating in the CP mode exhibit similar characteristics to those in the CW mode. CAORC and BORC share identical control ranges, maintaining a constant evaporation pressure of 1300 kPa for most of the time. When the $T_{\rm hf}$ falls below 102 °C (1847–2053 s), the systems switch to constant superheat mode. At this stage, the R236fa mass fraction in the CAORC reaches 1.0, precluding further adjustment. Only the mass flow rate of the working fluid can be regulated to maintain a constant superheat at 10 °C. As $T_{\rm hf}$ decreases, the mass flow rate of the CAORC gradually declines, approaching 756.69 kg/h during 1847–1950 s, as shown in Fig. 11 (b). When the temperature rises again (1950-2053 s), the CAORC system decreases the mass fraction of R123 in the working fluid to elevate the mass flow rate. Similar to the CW mode, MORC in the CP mode exhibits the narrowest control range, maintaining constant evaporation pressure only when $T_{\rm hf}$ exceeds 120 °C (1243-1657 s). Outside this range, it switches to constant superheat mode with significant evaporation pressure fluctuations, with the minimum recorded pressure reaching 923 kPa.

It is noted that the phenomenon that the BORC shows the same control range as the CAORC and the MORC exhibits a quite narrow control range is a relative term, which is closely related to the setting of the control objective: the output power of 3000W and the evaporation pressure of 1300 kPa. The results in Fig. 11 imply that the control range could be enlarged if the mass fraction of R236fa becomes higher for the MORC; otherwise, the control range tends to shrink until no control range is available or the mixture becomes pure R123. The change of the control objective will impose a significant effect on the control range of the BORC or MORC, while the CAORC holds the obvious advantage attributed to the active adjustment of the mixture concentration to be more adaptable to the fluctuation of the $T_{\rm hf}$.

Fig. 12 further compares parameter variations and the performance of ORC systems under the two control strategies. During the CW

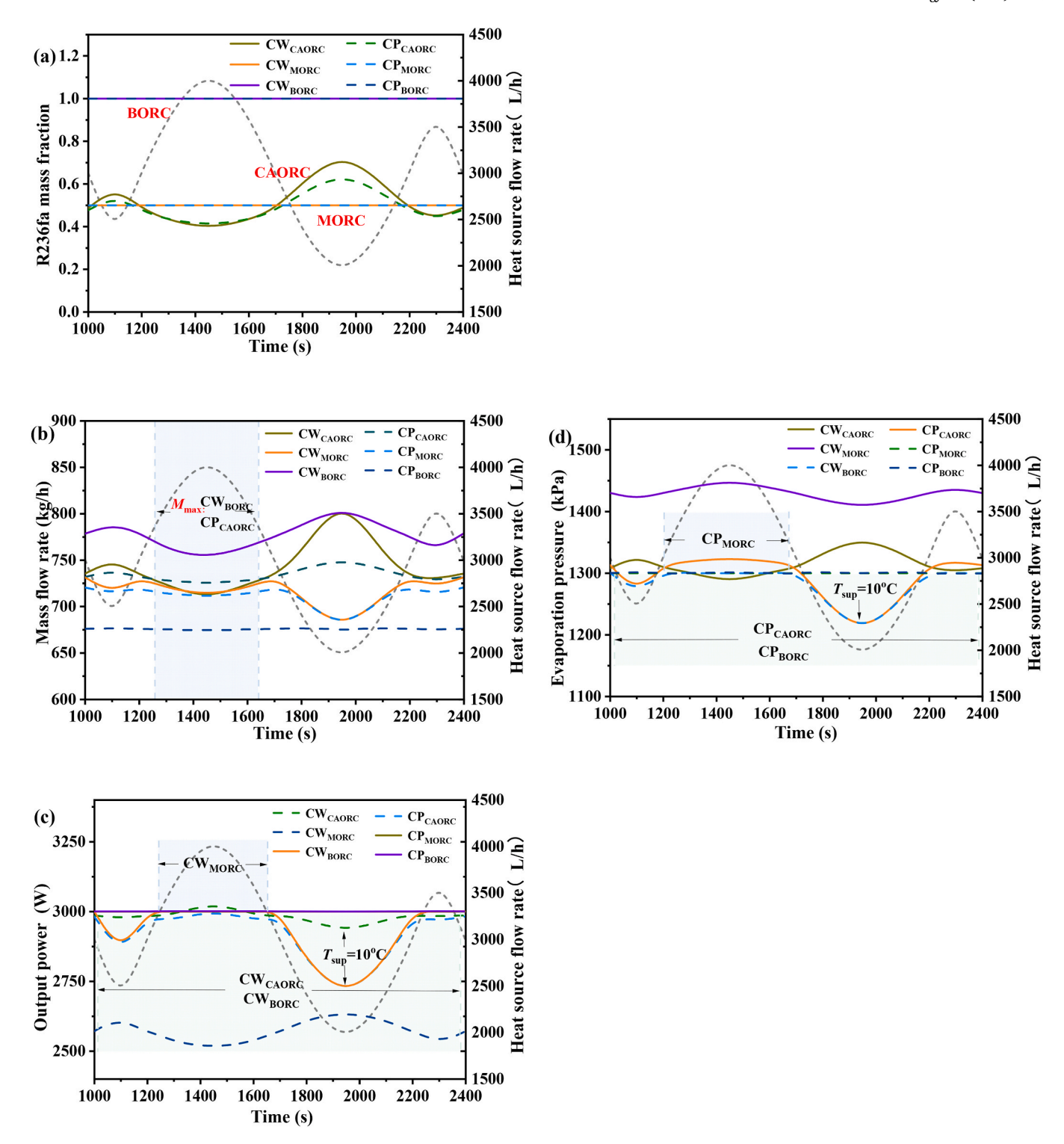


Fig. 13. Variation of control variables and objectives with time under the heat source mass flow rate fluctuation.

operation, CAORC exhibits the lowest evaporation and condensation pressures due to its minimal R236fa mass fraction (ranging from 0.2 to 0.5), as discussed in Section 3.1. This configuration also demonstrates the most pronounced temperature glide, reducing the heat transfer temperature difference as the evaporation temperature increases. Additionally, the superheat remains consistently as low as $10\,^{\circ}\text{C}$ through the active adjustment of the mass fraction of R236fa. In contrast, BORC and MORC in the CW mode primarily adjust mass flow rates to maintain constant power output but fail to actively reduce the vapor superheat. Consequently, these modes exhibit higher and more variable superheat

levels: 10–42.15 °C for BORC and 10–21.39 °C for MORC. Excessive superheat fluctuations degrade thermal match in heat exchangers and increase exergy losses. The CAORC is more adaptable to the fluctuation of the $T_{\rm hf}$, yielding a higher average thermal efficiency of 5.91 % and exergy efficiency of 27.82 % under the CW mode, seen in Table 8, compared to the average thermal efficiency of 5.61 % and exergy efficiency of 26.61 % for the BORC in their control range (1000–1777 s and 123–1645 s, the ORC system achieves the average thermal efficiency of 6.04 % and exergy efficiency of 26.44 % while the CAORC mode also

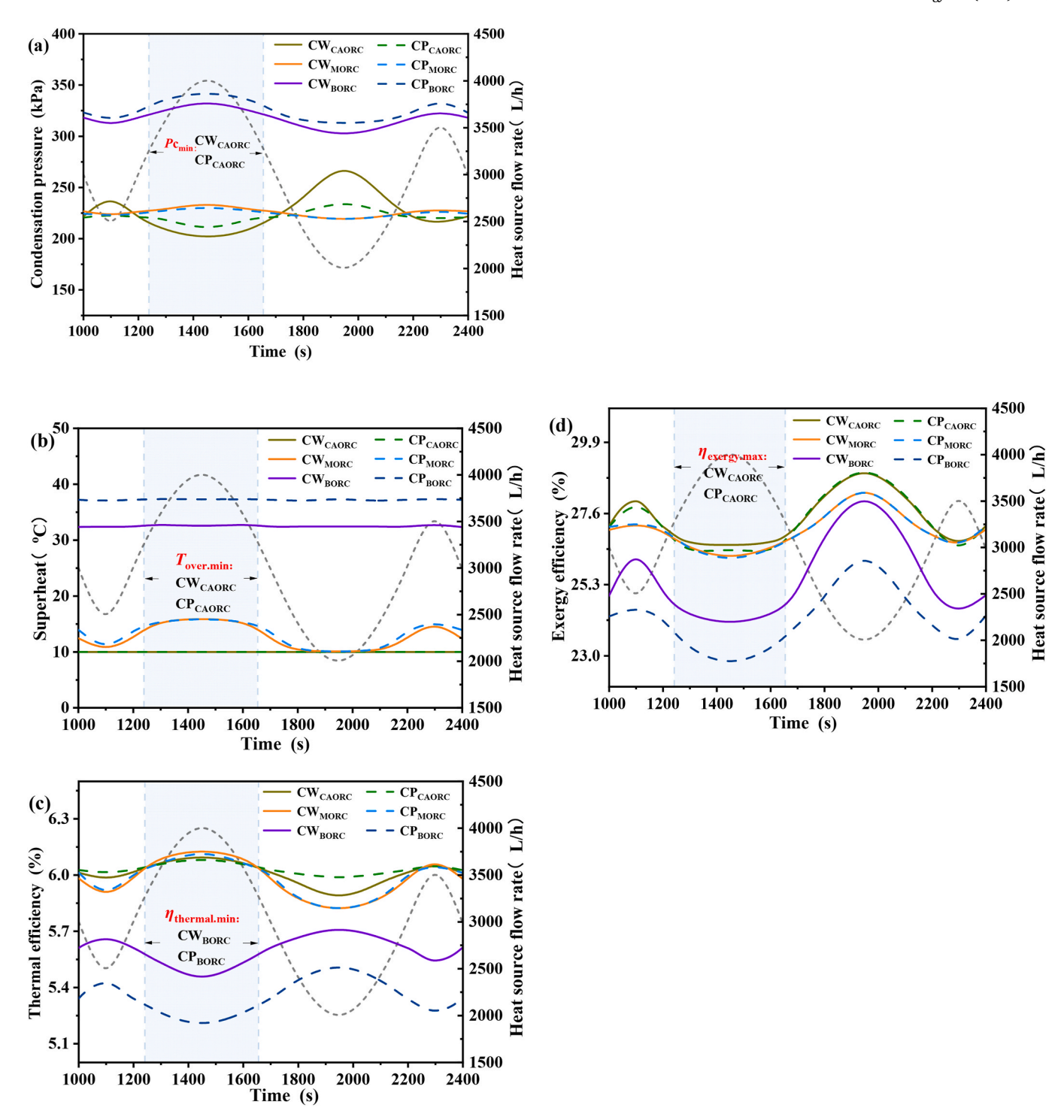


Fig. 14. Temporal variation of key parameters and system performance under the heat source mass flow rate fluctuation.

exhibits superior performance: the average thermal efficiency of $6.11\,\%$ and exergy efficiency of $26.62\,\%$. Similar trends are observed in the CP mode, where the CAORC maintains the lowest condensation pressure and most stable superheat of $10\,^\circ$ C, achieving peak thermal efficiency ($6.34\,\%$) and exergy efficiency ($26.52\,\%$) at $1450\,$ s. For the shared control range of 1243– $1657\,$ s, the CAORC in the CP mode shows the higher average thermal efficiency of $6.17\,\%$ and exergy efficiency of $26.86\,\%$ while the BORC has the average thermal efficiency of $5.37\,\%$ and exergy efficiency of $24.21\,\%$. Compared with the MORC in the CP mode in its control range of 1243– $1657\,$ s, the CAORC also achieves higher system performance: the average thermal efficiency of $6.17\,\%$

and exergy efficiency of 26.28 % while the MORC has the average thermal efficiency of 6.04 % and exergy efficiency of 26.44 %.

In summary, under the fluctuation of $T_{\rm hf}$, the CAORC has superior performance: the largest control range and the highest efficiencies, as well as stable vapor superheat degrees, ensuring operational safety. For the CW operation, the thermal efficiency of the CAORC is 9.17 % higher than the BORC and 1.15 % higher than the MORC, while the exergy efficiency of the CAORC is 8.34 % higher than the BORC and 0.68 % higher than the MORC. For the CP operation, the thermal efficiency of the CAORC is 12.97 % higher than the BORC and 2.6 % higher than the MORC, while the exergy efficiency of the CAORC is 9.87 % higher than

Table 9The control range and performance of different modes with heat source flow rate fluctuations.

Operation mode	Control range	Average thermal efficiency (under shared range with MORC)<	Average exergy efficiency (under shared range with MORC)
CW _{BORC}	1000–2400 s	5.60 % (5.55 %)	25.40 % (24.48 %)
CW_{MORC}	1200–1700 s	6.06 %	26.60 %
CW_{CAORC}	1000–2400 s	6.01 % (6.05 %)	27.33 % (26.86 %)
CP_{BORC}	1000–2400 s	5.34 % (5.29 %)	24.12 % (23.46 %)
CP_{MORC}	1200–1700 s	6.05 %	26.59 %
CP_{CAORC}	1000–2400 s	6.03 % (6.05 %)	27.28 % (26.66 %)

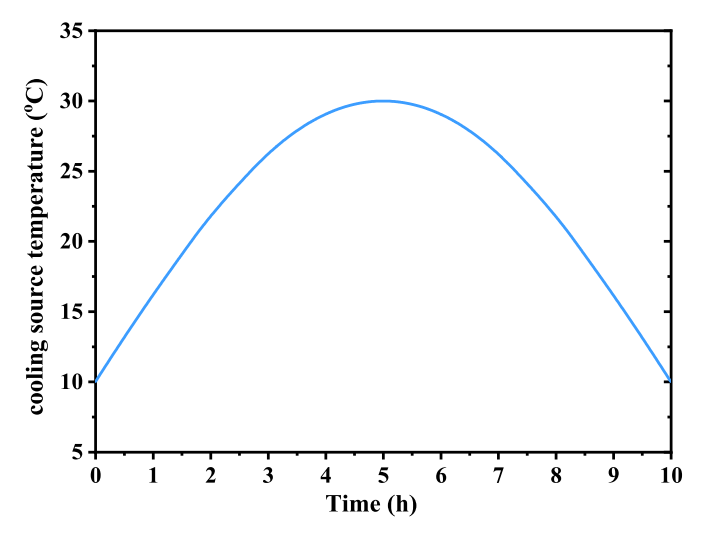


Fig. 15. Variation of cold source temperature with time.

the BORC and 0.89 % higher than the MORC.

3.2.2. Performance of the ORC with heat source flow rate fluctuations

As shown in Fig. 10, the $V_{\rm hf}$ varies, while other system parameters remain consistent with those mentioned above. Fig. 13 shows the variation of control variables and objectives over time, where the gray dashed line represents the fluctuations in $V_{\rm hf}$ with time. Fig. 13(a-b) illustrates that in the CAORC, the mass fraction of R236fa fluctuates between 0.4 and 0.7. In contrast, the mass fraction of R236fa in the BORC and the MORC remains stable at 1 and 0.5. Comparatively, the CAORC demonstrates superior adaptability to fluctuations in the V_{hf} by dynamically adjusting the mass fraction of R236fa. Although all three working fluids exhibit mass flow rate fluctuations under both operation strategies, their magnitudes are significantly smaller compared to those caused by $T_{\rm hf}$ variations, indicating lower sensitivity of ORC systems to $V_{\rm hf}$ changes. During the operation of the two operating strategies, the BORC and CAORC exhibit the highest mass flow rates, with the mass flow rate of the BORC fluctuating between 776 kg/h and 750 kg/h and that of the CAORC between 724 kg/h and 750 kg/h. Additionally, mass flow rate fluctuations are more pronounced under the CW operation than under the CP operation.

Fig. 13(c–d) compares the control effectiveness of three working fluids in ORC systems under the CW and CP operation. In the CW operation, the CAORC and BORC maintain stable power output throughout the simulation. However, the MORC exhibits the narrower control range, sustaining constant power output only when the $V_{\rm hf}$

exceeds 3200 L/h (approximately from 1200 to 1650 s), representing 32.14 % of the range achievable by the other two modes. Outside this range, the MORC switches to constant superheat operation, highlighting its limited adaptability to variations in $V_{\rm hf}$. A similar trend is observed under the CP operation. The CAORC and BORC can maintain stable evaporation pressure throughout the simulation, while the MORC operates within the narrower range (3200 L/h, approximately from 1200 to 1650 s), also 31.21 % of the other modes' range, and switches to constant superheat operation otherwise.

Fig. 14 highlights differences in key parameters and system performance under the CW and CP operations. Fig. 14(a-d) compares variations in other key parameters and system performance with time under the two control strategies. Since fluctuations in $T_{\rm hf}$ and $V_{\rm hf}$ both originate from disturbances on the heat source side, the observed parameter trends exhibit a certain degree of consistency. In CW and CP operations, the CAORC maintains the lowest and most stable superheat levels, consistently around 10 °C, while the MORC shows fluctuations of the superheat within the range from 10 °C to 15 °C. CW_{BORC} and CP_{BORC} demonstrate significantly higher vapor superheat levels, reaching approximately 32 °C and 37 °C, respectively. The excessive superheat indicates substantial irreversible losses during heat exchange, which in turn degrade overall thermodynamic performance. During these operations, the CAORC not only achieves the lowest superheat but also maintains lower condensation pressures, averaging 212.75 kPa and 217.31 kPa, respectively. In terms of thermodynamic performance, the CAORC achieves thermal and exergy efficiencies comparable to those of the MORC. Specifically, the MORC in the CW mode attains an average thermal efficiency of 6.06 % and an exergy efficiency of 26.60 % during the control range of 1200 s-1700 s, seen in Table 9, while the CAORC achieves 6.05 % and 26.86 %, respectively. In contrast, BORC exhibits the lowest performance among the evaluated configurations, with the highest superheat levels and reductions in average thermal and exergy efficiencies by 7.1 % and 5.23 % in the CW operation and 11.44 % and 11.58 % in the CP operation, compared to the CAORC.

In summary, under $V_{\rm hf}$ variations, the CAORC exhibits superior performance during both the CW and CP operations. These systems maintain greater parameter stability across a broader control range compared to MORC while achieving more effective superheat regulation. Moreover, the characteristics of both control strategies under mass flow rate variations closely align with those observed under temperature variations, as both scenarios stem from disturbances on the heat source side. Additionally, the system demonstrates lower sensitivity to fluctuations in $V_{\rm hf}$, further enhancing its adaptability and operational stability.

3.2.3. Performance of the ORC with cooling water temperature fluctuations

As shown in Fig. 15, the temperature of the cooling source is simulated to fluctuate within a range of 10 °C–30 °C, following the diurnal variations in ambient temperature, while $T_{\rm hf}$ remains constant at 120 °C. According to the dynamic characteristics of the ORC system, changes in cooling source temperature ($T_{\rm cool}$) have a negligible effect on the heat source side, and the evaporation pressure remains nearly stable. Therefore, only the CW operation strategy is simulated in this section.

Fig. 16 illustrates the temporal variations in control parameters. In the CW mode, the mass fraction of R236fa in the CAORC varies between 0.4 and 0.7, peaking at 0.7 at the 5 h mark, with a maximum mass flow rate of 857.07 kg/h observed. This indicates that the CAORC system dynamically adjusts the working fluid concentration in response to $T_{\rm cool}$ variations, thereby adapting to changing operating conditions and enhancing thermodynamic performance. In contrast, the mass fraction of R236fa in the BORC and MORC remains stable at 1.0 and 0.5. During operation, all three working fluids exhibit significant mass flow rate fluctuations: 702.75–857.07 kg/h for the BORC, 650.25–748.94 kg/h for the CAORC, and 669.43–850.36 kg/h for the MORC. Among these, the BORC shows the highest mass flow rates. Fig. 16 (c) demonstrates the power output control capabilities of the three modes under the CW operation. Both the CAORC and BORC successfully maintain stable

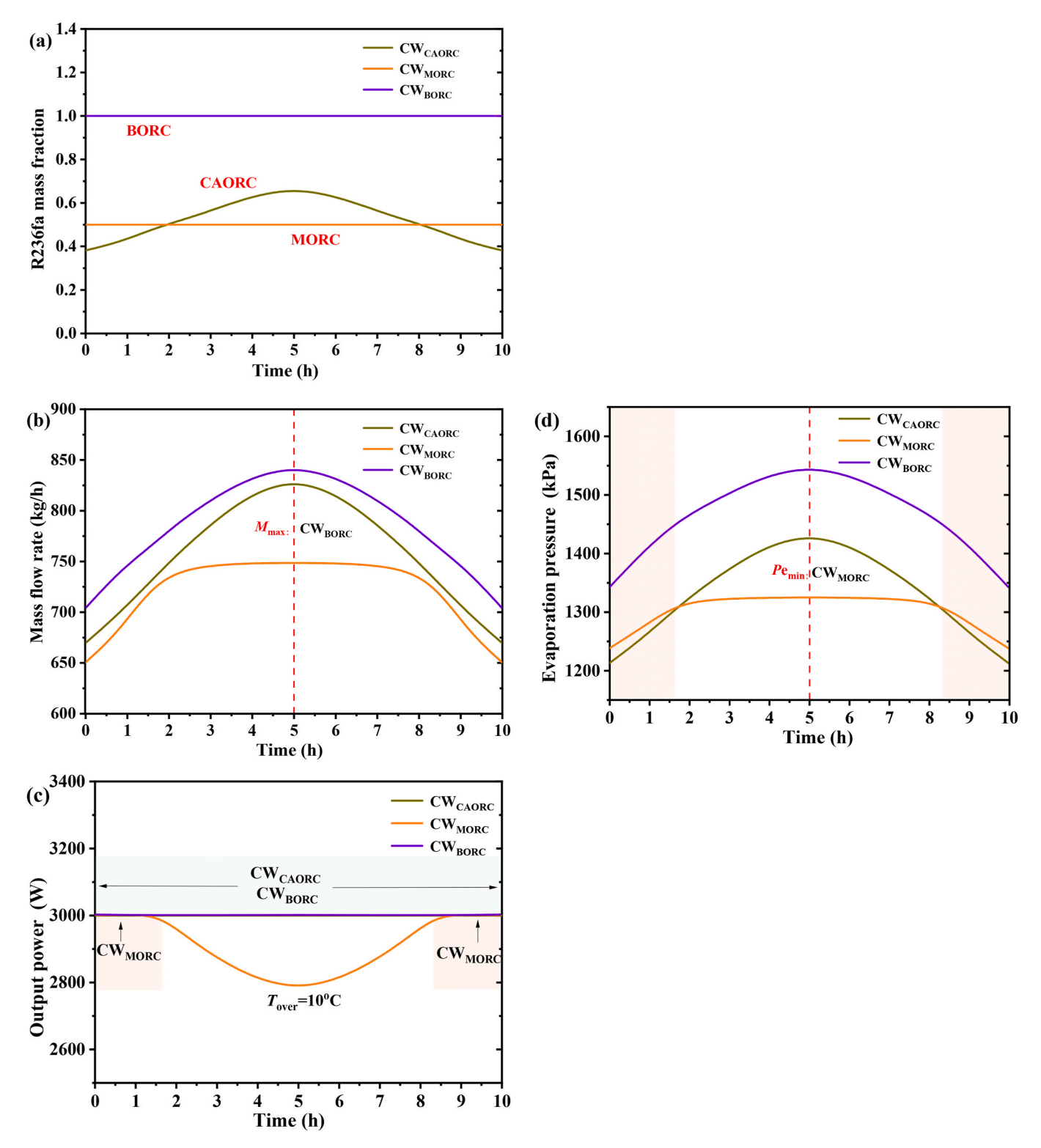


Fig. 16. Variation of control variables and objectives with time under the cooling source temperature fluctuation.

power output throughout the simulation. However, the MORC demonstrates a more constrained power control range, maintaining constant power output only within a narrow $T_{\rm cool}$ range from 10 °C to 18 °C. Outside this range, it switches to constant superheat mode, with power output fluctuating between 2800 W and 3000 W as the $T_{\rm cool}$ varies.

Fig. 17 highlights differences in key parameters and system performance under the CW operation. In the CAORC and BORC, both the evaporation and condensation pressures exhibit substantial fluctuations.

When the R236fa mass fraction of the CAORC is below 0.5, the evaporation pressure of the CAORC is lower than that of MORC. However, as the temperature of the cooling source rises, the evaporation pressure of the CAORC gradually increases and eventually surpasses that of the MORC. A similar trend is observed for condensation pressure. The degree of vapor superheat in the CAORC remains stable at 10 $^{\circ}$ C, whereas that in the MORC varies with the $T_{\rm cool}$. When the $T_{\rm cool}$ exceeds 18 $^{\circ}$ C, the MORC operates in constant superheat mode due to its inability to

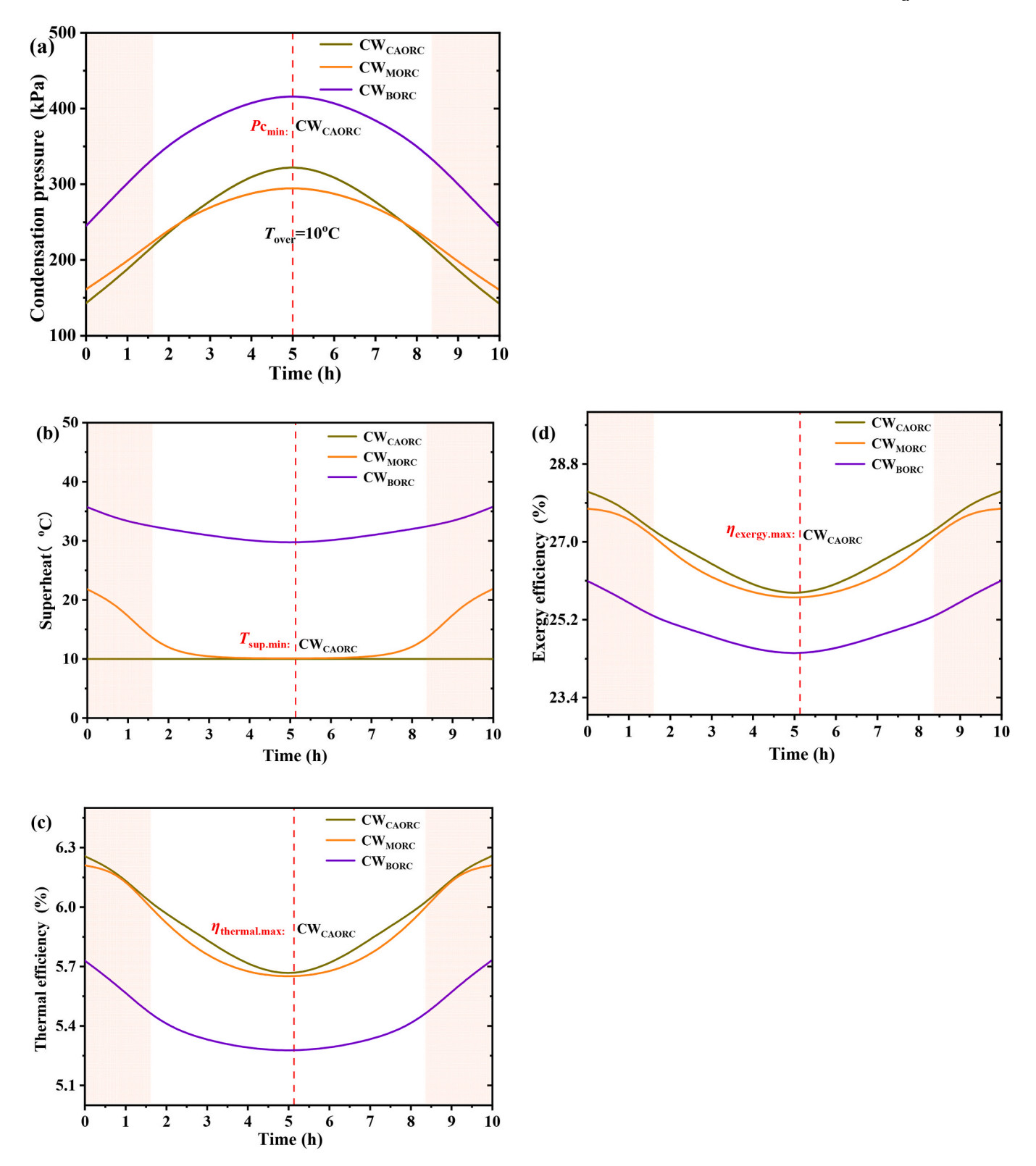


Fig. 17. Temporal variation of key parameters and system performance under the cooling source temperature fluctuation.

maintain stable output power. Regarding efficiency, both the CAORC and MORC exhibit comparable thermal and exergy efficiencies, fluctuating between 5.56 %-6.26 % and 25.34 %–28.15 %, respectively. While the CAORC demonstrates higher average efficiencies over a range of $T_{\rm cool}$, as shown in Table 10, with average thermal and exergy efficiencies of 6.02 % and 27.23 %, respectively. The MORC achieves thermal and exergy efficiencies of 5.99 % and 26.99 %. In contrast, the BORC

consistently operates with high superheat levels (>30 $^{\circ}$ C), leading to the absorption of the most heat but resulting in the lowest average thermal efficiency of 5.47 % and exergy efficiencies of 25.32 %, about 8.80 % and 7.34 % lower than the CAORC.

In summary, under $T_{\rm cool}$ variations, the CAORC also demonstrates superior performance during operation, maintaining stable power output and vapor superheat degrees throughout the simulation. The

Table 10The control range and thermodynamic performance of different modes with cooling water temperature fluctuations.

Operation mode	Control range	Average thermal efficiency (reduction compared to CAORC)	Average exergy efficiency (reduction compared to CAORC)
CW_{BORC}	0–1.67 h and 8.33–10 h	5.47 % (8.80 %)	25.32 % (7.34 %)
CW_{MORC} CW_{CAORC}	0–10 h 0–10 h	5.99 % (0.50 %) 6.02 %	26.99 % (0.88 %) 27.23 %

MORC exhibits a narrower control range and lower efficiencies, while the BORC shows the lowest efficiencies.

4. Conclusion

A dynamic model is established in this work for a 4 kW ORC prototype in the laboratory to study the transient behavior and develop the control strategy of the ORC system with concentration regulation of the mixture working fluid, R236fa/R123. The influence of the mixture working fluid on the system performance is discussed, and two control strategies are proposed and compared: constant output power operation and constant evaporation pressure operation. The main conclusions are as follows:

- (1) Compared to the temperature glide of mixture working fluids during phase change, a more significant effect of the concentration regulation is the variation of the average evaporation and condensation temperatures, which exhibits opposing effects on the heat transfer temperature differences in the evaporator and condenser. The trade-off between the exergy destruction of the evaporator and condenser results in the optimal system performance at a specific mixture concentration. At the Thf of 120 °C, the R236fa mass fraction of 0.6 shows a 6.3 % increase in thermal efficiency and a 6.2 % improvement in exergy efficiency, accompanied by a 5 % rise in power output compared to the pure R236fa.
- (2) Introducing the mixture concentration as the other control variable, alongside the mixture mass flow rate, enables dual-objective control of the system, realizing simultaneous stabilization of both the superheat degree and system output power under the CW mode or both the ORC evaporation pressure and superheat degree under the CP mode. Under the fluctuation of $T_{\rm hf}$, $V_{\rm hf}$, and $T_{\rm cool}$, the vapor superheat at the expander inlet is controlled at 10 °C. The CAORC exhibits superior performance in both CW and CP operations compared to the MORC and BORC in two aspects: the enlargement of the effective control range and the improvement of the system performance in terms of exergy efficiency and thermal efficiency.
- (3) Under heat source temperature fluctuation, the control range of the CAORC is comparable to the BORC and 3.3 times wider than the MORC. Besides, the CAORC achieves the highest thermal and exergy efficiencies. Specifically, for the CW operation, CAORC shows a thermal efficiency improvement of 9.17 % over BORC and 1.15 % over MORC, while exergy efficiency increases by 8.34 % and 0.68 %, respectively. For the CP operation, CAORC outperforms BORC and MORC by 12.97 % and 2.6 % in thermal efficiency, and by 9.87 % and 0.89 % in exergy efficiency, respectively.
- (4) Under heat source mass flow rate fluctuations, the CAORC achieves the widest control range under both CW and CP operations, which is approximately three times that of the MORC. During the shared range, the CAORC reaches an average thermal efficiency of 6.05 % and exergy efficiency of 26.86 % under the CW mode, which is comparable to the MORC (6.06 %, 26.60 %) and significantly higher than the BORC (5.55 %, 24.48 %). Similar

- trends are observed under the CP operation: the CAORC achieves 6.05 % thermal efficiency and 26.66 % exergy efficiency within the shared control range with the MORC, outperforming the BORC by 14.56 % in thermal efficiency and 13.64 % in exergy efficiency, respectively.
- (5) Under cooling water temperature fluctuations ranging from 10 °C to 30 °C, the CAORC maintains a wide control range (0–10 h) with stable power output and consistent vapor superheat (10 °C), which is about three times that of the MORC. The CAORC dynamically adjusts the R236fa mass fraction (0.4–0.7) and achieves the highest average thermal and exergy efficiencies at 6.02 % and 27.23 %, comparable to the MORC (average thermal and exergy efficiencies of 5.99 % and 26.99 %). The BORC system operates with the lowest average thermal efficiency of 5.47 % and exergy efficiencies of 25.32 %, about 8.80 % and 7.34 % lower than the CAORC.

It is noted that the current research is confined to the R236fa/R123 mixture, and the robustness of the dual-variable control strategy under extreme operating conditions (e.g., heat source fluctuations exceeding 30 %) requires further verification. To address these limitations, future work will prioritize the investigation of environmentally friendly HFO-based refrigerants to enhance the findings.

CRediT authorship contribution statement

Zheng Miao: Writing – original draft, Supervision, Conceptualization. Yuchen Zhang: Writing – original draft, Investigation. Peiwei Yan: Software, Methodology. Jinliang Xu: Validation, Data curation.

Declaration of competing interest

The authors declare that they have no known competing financial interests or personal relationships that could have appeared to influence the work reported in this paper.

Acknowledgments

The authors are grateful to the National Natural Science Foundation of China (No. 52476007) for the assistance.

Data availability

Data will be made available on request.

References

- Friedlingstein P, O'Sullivan M, Jones MW, Andrew RM, Hauck J, Landschützer P, et al. Global carbon budget 2024. Earth Syst Sci Data 2025;17(3):965–1039. https://doi.org/10.5194/essd-17-965-2025.
- [2] Tollefson J. IPCC says limiting global warming to 1.5 °C will require drastic action. Nature 2018;562(7726):172–3.
- [3] Yan D, Yang FB, Yang FF, Zhang HG, Guo ZY, Li JA, et al. Identifying the key system parameters of the organic Rankine cycle using the principal component analysis based on an experimental database. Energy Convers Manag 2021;240: 114252. https://doi.org/10.1016/j.enconman.2021.114252.
- [4] Frate GF, Baccioli A, Lucchesi E, Ferrari L. ORC optimal design through clusterization for waste heat recovery in anaerobic digestion plants. Appl Sci-Basel 2021;11(6):2762. https://doi.org/10.3390/app11062762.
- [5] Braimakis K, Karellas S. Exergetic optimization of double stage organic rankine cycle (ORC). Energy 2018;149:296–313. https://doi.org/10.1016/j. energy.2018.02.044.
- [6] Akbari S, Faghiri S, Zinjanabi AM, Bijarchi MA, Shafii MB, Hosseinzadeh K. Thermo-economic investigation and comparative multi-objective optimization of dual-pressure evaporation ORC using binary zeotropic mixtures as working fluids for geothermal energy application. International Journal of Thermofluids 2024;24. https://doi.org/10.1016/j.iifr.2024.100809
- https://doi.org/10.1016/j.ijft.2024.100899.
 Feng Y-q, Xu K-j, Liu Z-x, Yu H-s, Hung T-C, He Z-x. Construction and preliminary test of a biomass-fired organic Rankine cycle system for heat and power system.
 Energy 2024;308. https://doi.org/10.1016/j.energy.2024.133021.

- [8] Liu P, Shu GQ, Tian H. How to approach optimal practical Organic Rankine cycle (OP-ORC) by configuration modification for diesel engine waste heat recovery. Energy 2019;174:543–52. https://doi.org/10.1016/j.energy.2019.03.016.
- [9] Ping X, Yang FB, Zhang HG, Zhang J, Zhang WJ, Song GG. Introducing machine learning and hybrid algorithm for prediction and optimization of multistage centrifugal pump in an ORC system. Energy 2021;222:120007. https://doi.org/ 10.1016/j.energy.2021.120007.
- [10] Bekiloglu HE, Bedir H, Anlas G. Multi-objective optimization of ORC parameters and selection of working fluid using preliminary radial inflow turbine design. Energy Convers Manag 2019;183:833–47. https://doi.org/10.1016/j. enconman.2018.12.039.
- [11] Lu P, Chen K, Luo X, Wu W, Liang Y, Chen J, et al. Experimental and simulation study on a zeotropic ORC system using R1234ze(E)/R245fa as working fluid. Energy 2024;292. https://doi.org/10.1016/j.energy.2024.130453.
- [12] Fiaschi D, Manfrida G, Maraschiello F. Thermo-fluid dynamics preliminary design of turbo-expanders for ORC cycles. Appl Energy 2012;97:601–8. https://doi.org/ 10.1016/j.apenergy.2012.02.033.
- [13] Mosaffa AH, Farshi LG. Thermodynamic feasibility evaluation of an innovative salinity gradient solar ponds-based ORC using a zeotropic mixture as working fluid and LNG cold energy. Appl Therm Eng 2021;186:116488. https://doi.org/ 10.1016/j.applthermaleng.2020.116488.
- [14] Bao J, Zhao L. A review of working fluid and expander selections for organic Rankine cycle. Renew Sustain Energy Rev 2013;24:325–42. https://doi.org/ 10.1016/j.rser.2013.03.040.
- [15] Habka M, Ajib S. Evaluation of mixtures performances in Organic Rankine Cycle when utilizing the geothermal water with and without cogeneration. Appl Energy 2015;154:567–76. https://doi.org/10.1016/j.apenergy.2015.05.046.
- [16] Kang Z, Zhu J, Lu X, Li T, Wu X. Parametric optimization and performance analysis of zeotropic mixtures for an organic Rankine cycle driven by low-medium temperature geothermal fluids. Appl Therm Eng 2015;89:323–31. https://doi.org/ 10.1016/j.applthermaleng.2015.06.024.
- [17] Li T, Zhu J, Fu W, Hu K. Experimental comparison of R245fa and R245fa/R601a for organic Rankine cycle using scroll expander. Int J Energy Res 2015;39(2): 202–14. https://doi.org/10.1002/er.3228.
- [18] Yang M-H, Yeh R-H. Performance improvement of the ocean thermal energy conversion using R1234ZEZ/R1233ZDE in an organic Rankine cycle. Energy 2025; 327. https://doi.org/10.1016/j.energy.2025.136403.
- [19] Liu F, Yang C, Li B, Silang Y, Zhu Y, Farkoush SG. Thermodynamic and economic sensitivity analyses of a geothermal-based trigeneration system; performance enhancement through determining the best zeotropic working fluid. Energy 2022; 246. https://doi.org/10.1016/j.energy.2022.123310.
- [20] Xia X, Zhang H, Wang Z, Yang C, Sun T, Peng B. Performance comparison of two ORC-VCR system configurations using pure/mixture working fluids based on multiobjective optimization. Appl Therm Eng 2024;255. https://doi.org/10.1016/j. applthermaleng.2024.124027.
- [21] Feng Y-q, Hung T-C, He Y-L, Wang Q, Wang S, Li B-x, et al. Operation characteristic and performance comparison of organic Rankine cycle (ORC) for low-grade waste heat using R245fa, R123 and their mixtures. Energy Convers Manag 2017;144: 153–63. https://doi.org/10.1016/j.enconman.2017.04.048.
- [22] Chen H, Goswami DY, Rahman MM, Stefanakos EK. A supercritical Rankine cycle using zeotropic mixture working fluids for the conversion of low-grade heat into power. Energy 2011;36(1):549–55. https://doi.org/10.1016/j. energy 2010.10.006
- [23] Radulovic J, Beleno Castaneda NI. On the potential of zeotropic mixtures in supercritical ORC powered by geothermal energy source. Energy Convers Manag 2014;88:365–71. https://doi.org/10.1016/j.enconman.2014.08.048.
- [24] Vivian J, Manente G, Lazzaretto A. A general framework to select working fluid and configuration of ORCs for low-to-medium temperature heat sources. Appl Energy 2015;156:727–46. https://doi.org/10.1016/j.apenergy.2015.07.005.
- [25] Zhao L, Bao J. Thermodynamic analysis of organic Rankine cycle using zeotropic mixtures. Appl Energy 2014;130:748–56. https://doi.org/10.1016/j. apenergy.2014.03.067.
- [26] Pang K-C, Chen S-C, Hung T-C, Feng Y-Q, Yang S-C, Wong K-W, et al. Experimental study on organic Rankine cycle utilizing R245fa, R123 and their mixtures to investigate the maximum power generation from low-grade heat. Energy 2017; 133:636–51. https://doi.org/10.1016/j.energy.2017.05.128.

- [27] Bamorovat Abadi G, Yun E, Kim KC. Experimental study of a 1 kw organic Rankine cycle with a zeotropic mixture of R245fa/R134a. Energy 2015;93:2363–73. https://doi.org/10.1016/j.energy.2015.10.092.
- [28] Wang Z, Zhang S, Xia X, Zhao Y, Yi Q, Zhang X. Experimental study on dynamic characteristics of organic Rankine cycle coupled vapor compression refrigeration system with a zeotropic mixture. Energy 2024;307. https://doi.org/10.1016/j. energy 2024.132726
- [29] Chen X, Liu C, Li Q, Wang X, Xu X. Dynamic analysis and control strategies of Organic Rankine Cycle system for waste heat recovery using zeotropic mixture as working fluid. Energy Convers Manag 2019;192:321–34. https://doi.org/10.1016/ i.encomman.2019.04.049.
- [30] Lu P, Luo X, Wang J, Chen J, Liang Y, Yang Z, et al. Thermo-economic design, optimization, and evaluation of a novel zeotropic ORC with mixture composition adjustment during operation. Energy Convers Manag 2021;230. https://doi.org/ 10.1016/j.encomman.2020.113771.
- [31] Liu C, Gao T. Off-design performance analysis of basic ORC, ORC using zeotropic mixtures and composition-adjustable ORC under optimal control strategy. Energy 2019;171:95–108. https://doi.org/10.1016/j.energy.2018.12.195.
- [32] Collings P, Yu Z, Wang E. A dynamic organic Rankine cycle using a zeotropic mixture as the working fluid with composition tuning to match changing ambient conditions. Appl Energy 2016;171:581–91. https://doi.org/10.1016/j. apenergy.2016.03.014.
- [33] Wang E, Yu Z, Collings P. Dynamic control strategy of a distillation system for a composition-adjustable organic Rankine cycle. Energy 2017;141:1038–51. https:// doi.org/10.1016/j.energy.2017.09.141.
- [34] Wei DH, Lu XS, Lu Z, Gu JM. Performance analysis and optimization of organic Rankine cycle (ORC) for waste heat recovery. Energy Convers Manag 2007;48(4): 1113–9. https://doi.org/10.1016/j.enconman.2006.10.020.
- [35] Imran M, Pili R, Usman M, Haglind F. Dynamic modeling and control strategies of organic Rankine cycle systems: methods and challenges. Appl Energy 2020;276:28. https://doi.org/10.1016/j.apenergy.2020.115537.
- [36] Kuo WS, Lie YM, Hsieh YY, Lin TF. Condensation heat transfer and pressure drop of refrigerant R-410A flow in a vertical plate heat exchanger. Int J Heat Mass Tran 2005;48(25–26):5205–20.
- [37] Han D-H, Lee K-J, Kim Y-H. Experiments on the characteristics of evaporation of R410A in brazed plate heat exchangers with different geometric configurations. Appl Therm Eng 2003;23(10):1209–25. https://doi.org/10.1016/s1359-4311(03) 00061-9
- [38] Wang J, Wang M, Li M, Xia J, Dai Y. Multi-objective optimization design of condenser in an organic Rankine cycle for low grade waste heat recovery using evolutionary algorithm. Int Commun Heat Mass Tran 2013;45:47–54. https://doi. org/10.1016/j.icheatmasstransfer.2013.04.014.
- [39] Das SK, Spang B, Roetzel W. Dynamic behavior of plate heat exchangers—experiments and modeling. J Heat Tran 1995;117(4):859–64.
- [40] Yi-Yie Yan, Hsiang-Chao Lio, et al. Condensation heat transfer and pressure drop of refrigerant R-134a in a plate heat exchanger. Int J Heat Mass Tran 1999;42(6): 993–1006.
- [41] Lemort V, Quoilin S, Cuevas C, Lebrun J. Testing and modeling a scroll expander integrated into an Organic Rankine Cycle. Appl Therm Eng 2009;29(14–15): 3094–102. https://doi.org/10.1016/j.applthermaleng.2009.04.013.
- [42] Quoilin S, Lemort V, Lebrun J. Experimental study and modeling of an Organic Rankine Cycle using scroll expander. Appl Energy 2010;87(4):1260–8. https://doi. org/10.1016/j.apenergy.2009.06.026.
- [43] Feng YQ, Hung TC, Wu SL, Lin CH, Li BX, Huang KC, et al. Operation characteristic of a R123-based organic Rankine cycle depending on working fluid mass flow rates and heat source temperatures. Energy Convers Manag 2017;131:55–68. https:// doi.org/10.1016/j.enconman.2016.11.004.
- [44] Jiménez-Arreola M, Wieland C, Romagnoli A. Direct vs indirect evaporation in Organic Rankine Cycle (ORC) systems: a comparison of the dynamic behavior for waste heat recovery of engine exhaust. Appl Energy 2019;242:439–52. https://doi. org/10.1016/j.apenergy.2019.03.011.
- [45] Yu X, Huang Y, Li Z, Huang R, Chang J, Wang L. Characterization analysis of dynamic behavior of basic ORC under fluctuating heat source. Appl Therm Eng 2021;189:116695. https://doi.org/10.1016/j.applthermaleng.2021.116695.